

1

2 Enhanced understanding of atmospheric blocking modulation on ozone  
3 dynamics within a high-resolution Earth system model

4 Wenbin Kou<sup>1</sup>, Yang Gao<sup>1\*</sup>, Dan Tong<sup>2</sup>, Xiaojie Guo<sup>3,4</sup>, Xiadong An<sup>5</sup>, Wenyu Liu<sup>2</sup>, Mengshi Cui<sup>2</sup>,  
5 Xiuwen Guo<sup>1</sup>, Shaoqing Zhang<sup>6</sup>, Huiwang Gao<sup>1</sup>, Lixin Wu<sup>6</sup>

6

7 <sup>1</sup>Frontiers Science Center for Deep Ocean Multispheres and Earth System and Key Laboratory of  
8 Marine Environmental Science and Ecology, Ministry of Education, Ocean University of China,  
9 and Laoshan Laboratory, Qingdao, 266100, China

10 <sup>2</sup>Department of Earth System Science, Tsinghua University, Beijing, 100084, China

11 <sup>3</sup>International Center for Climate and Environment Sciences, Institute of Atmospheric Physics,  
12 Chinese Academy of Sciences, Beijing, 100029, China

13 <sup>4</sup>University of Chinese Academy of Sciences, Beijing, 100049, China

14 <sup>5</sup>College of Oceanic and Atmospheric Sciences, Ocean University of China, Qingdao, 266100,  
15 China

16 <sup>6</sup>Frontiers Science Center for Deep Ocean Multispheres and Earth System, and Key Laboratory of  
17 Physical Oceanography, Ministry of Education, the College of Oceanic and Atmospheric Sciences,  
18 Ocean University of China, and Laoshan Laboratory, Qingdao, 266100, China

19

20 \*Correspondence to: [yanggao@ouc.edu.cn](mailto:yanggao@ouc.edu.cn)

21

22

23

24

25

26

27

28

29

30

31

32

33

## Abstract

34 High surface ozone concentrations of surface ozone pose significant substantial  
35 health risks, yet understanding the factors governing influencing ozone levels,  
36 particularly especially the influence role of large-scale circulations, remains incomplete.  
37 A key challenge lies in accurately modeling both large-scale circulations and ozone  
38 concentrations. Leveraging recent advancements in optimizing Using a high-resolution  
39 Earth system model with (25 km atmospheric resolution), we explore how local  
40 meteorology and large-scale circulations impact affect ozone concentrations is  
41 investigated. We find levels. Our results show that heatwaves can trigger substantial  
42 increases in ozone concentrations by stimulating biogenic volatile organic compound  
43 (BVOC) emissions during the summers of 2015-2019. For example, compared to non-  
44 heatwave periods, maximum daily 8-h (MDA8) ozone concentrations during heatwaves  
45 increase by 12.0 ppbv in the southeastern U.S., 9.7 ppbv in Europe, 17.6 ppbv in North  
46 China, and 9.0 ppbv in central eastern China, compared to non-heatwave periods. In  
47 addition to local effects, atmospheric blocking strongly influences downstream  
48 meteorological conditions and ozone formation. Focusing on ozone pollution in eastern  
49 China, we identify three major pathways of Rossby wave propagation based on  
50 blocking locations: the Euro-Atlantic sector, northern Russia, and the North Pacific,  
51 inducing. These pathways lead to increased air temperature and intensified downward  
52 surface solar radiation downstream. The impact of blocking is most pronounced ever in  
53 central eastern China, where MDA8 ozone concentrations during blocking increase by  
54 5.9 ppbv to 10.7 ppbv during blocking, compared to reference non-blocking periods,  
55 followed by North China, ranging from (2.1 ppbv to 4.9 ppbv). Blocking can also  
56 stimulate more BVOC emissions, enhancing MDA8 ozone concentrations by 10.6 ppbv  
57 to 15.9 ppbv. in these regions. These findings underscore highlight the critical role that of  
58 large-scale atmospheric circulation patterns play in shaping regional seale air quality,  
59 particularly especially under a warming climate.

60

61 Key words: atmospheric blocking, ozone, Rossby wave propagation, BVOC emissions

62

63

64

65 **Summary**

66 Unlike traditional numerical studies, we apply a high-resolution Earth system model,  
67 improving simulations of surface ozone and large-scale circulations such as  
68 atmospheric blocking. In addition to local heatwave effects, we quantify the impact of  
69 atmospheric blocking on downstream ozone concentrations, which is closely associated  
70 with the blocking position. We identify three major pathways of Rossby wave  
71 propagation, stressing the critical role of large-scale circulation play in regional air  
72 quality.

73

74 **1. Introduction**

75 Air pollution ranks as the fourth leading global risk factor for mortality, trailing high  
76 systolic blood pressure, tobacco use, and dietary risks (Brauer et al., 2021)(Brauer et  
77 al., 2021). Among atmospheric pollutants, ~~ambient~~ ozone is ~~a major an important~~  
78 contributor to this burden (Fuller et al., 2022), affecting human health (Nuvolone et al.,  
79 2018)(Nuvolone et al., 2018), global climate (Deitrick and Goldblatt, 2023), and  
80 ecosystem health through exacerbating crop yield losses (Emberson et al., 2018).

域代码已更改

81 The HTAP (Hemispheric Transport of Air Pollution; (Dentener et al., 2010; Parrish  
82 et al., 2012)) and TOAR (Tropospheric Ozone Assessment Report; (Tarasick et al.,  
83 2019)) programs have extensively studied long-term ozone trends. Their synthesis in  
84 2021 (Parrish et al., 2021b)(Parrish et al., 2021b) reveals a twofold increase in lower  
85 tropospheric ozone at northern mid-latitudes from 1950 to 2000. The World Health  
86 Organization (WHO) strengthened air quality standards in 2021, emphasizing the  
87 critical need to assess ozone trends and their key drivers.

88 Ozone, a secondary air pollutant, forms when emission precursors such as volatile  
89 Organic Compounds (VOCs) and NO<sub>x</sub> are present (Fu and Tian, 2019).(Fu and Tian,  
90 2019). While anthropogenic emissions are significant, biogenic VOC (BVOC)  
91 emissions, which comprise about 90% of global VOC emissions (Guenther et al.,  
92 2012)(Guenther et al., 2012), are particularly sensitive to temperature. For instance,  
93 BVOC emissions notably elevate ~~surface~~ ozone levels in the North China Plain,  
94 particularly at surface, contributing to increases of 7.8 ppbv and 10.0 ppbv in the  
95 regional average maximum daily 8-h (MDA8) ozone concentrations in the North China  
96 Plain and Beijing, respectively, during the summer of 2017 (Ma et al., 2019).(Ma et al.,  
97 2019). Please note that unless otherwise specified, ozone in this study refers to surface  
98 ozone. Even in less polluted regions such as the U.S., BVOC emissions contribute a  
99 notable fraction of ozone, averaging 10% and 19% in the western and southeastern U.S.,  
100 respectively (Zhang et al., 2017).

101 This effect is amplified under favorable meteorological conditions. Compared to  
102 non-heatwave periods, heatwaves trigger increased BVOC emissions, resulting in

103 regional daytime ozone concentration increases of  $10 \mu\text{g m}^{-3}$  in the Pearl River Delta,  
104 with peaks reaching  $42.1 \mu\text{g m}^{-3}$  (Wang et al., 2021). In southwestern Europe,  
105 heatwaves induce a 33% rise in BVOC emissions, resulting in ~~surface ozone~~  
106 ~~concentration increases of  $9 \mu\text{g m}^{-3}$  during the summers of 2012-2014~~ (Guion et al.,  
107 ~~2023), ozone concentration increases of  $9 \mu\text{g m}^{-3}$  during the summers of 2012-2014~~  
108 (Guion et al., 2023). However, biases in modeling heatwaves (Gao et al., 2012)(Gao et  
109 al., 2012) and ozone, such as overestimations up to 20 ppbv in low-resolution global  
110 models (Emmons et al., 2020; Lamarque et al., 2012), have hindered previous  
111 investigations, primarily conducted using regional weather and chemistry models (Gao  
112 et al., 2020; Zhang et al., 2022). Addressing these challenges, especially the biases from  
113 low-resolution global models in boundary conditions (Zeng et al., 2022), is crucial for  
114 advancing Earth system models to better understand the impact of heatwaves on ozone  
115 through BVOC emissions.

116 ~~Local meteorological factors, particularly high temperatures, are closely linked to~~  
117 ~~large-scale circulations (Li and Sun, 2018), which further influence the ozone-~~  
118 ~~temperature relationship. For instance, the correlation between summer surface ozone~~  
119 ~~and temperature over eastern North America correlates with the position of the jet~~  
120 ~~stream, defined by the latitude of the maximum 500 hPa zonal wind averaged across~~  
121 ~~the region (Barnes and Fiore, 2013). Atmospheric circulations, such as the North~~  
122 ~~Atlantic Oscillation, significantly affect moisture transport, precipitation, and~~  
123 ~~subsequently, trace gas transport, deposition and air pollutant concentrations~~  
124 (Christoudias et al., 2012). In central eastern China, the East Asian summer monsoon  
125 ~~explains 2%–5% of interannual variations in surface ozone concentrations (Yang et al.,~~  
126 ~~2014). Moreover, a positive phase of the Eurasian teleconnection induces Rossby wave~~  
127 ~~train propagation from Europe to North China, influencing downward surface solar~~  
128 ~~radiation intensity and temperatures, thereby modulating ozone concentration~~  
129 ~~variability (Yin et al., 2019).~~

130 ~~Recently, Yang et al. (2022) Local meteorological factors, particularly high~~  
131 ~~temperatures, are closely linked to large-scale circulations (Li and Sun, 2018), which~~

132 [further influence the ozone-temperature relationship. For instance, the correlation](#)  
133 [between summer ozone and temperature over eastern North America correlates with the](#)  
134 [position of the jet stream, defined by the latitude of the maximum 500 hPa zonal wind](#)  
135 [averaged across the region \(Barnes and Fiore, 2013\). Atmospheric circulations, such as](#)  
136 [the North Atlantic Oscillation, significantly affect moisture transport, precipitation, and](#)  
137 [subsequently, trace gas transport, deposition and air pollutant concentrations](#)  
138 [\(Christoudias et al., 2012\). In central eastern China, the East Asian summer monsoon](#)  
139 [explains 2%-5% of interannual variations in ozone concentrations \(Yang et al., 2014\).](#)  
140 [Moreover, a positive phase of the Eurasian teleconnection induces Rossby wave train](#)  
141 [propagation from Europe to North China, influencing downward surface solar radiation](#)  
142 [intensity and temperatures, thereby modulating ozone concentration variability \(Yin et](#)  
143 [al., 2019\).](#)

144 [Recently, Yang et al. \(2022\) highlighted that high temperatures alone may not](#)  
145 [always enhance ozone formation](#)<sup>145</sup>[. For instance, high temperatures induced by a zonal](#)  
146 ['+ - +' wave-train pattern over Eurasia at 300 hPa may not favor ozone enhancement in](#)  
147 [North China. In contrast, circulation anomalies resembling an atmospheric blocking](#)  
148 [pattern, including positive geopotential height anomalies at 300 hPa over North China](#)  
149 [and eastern Eurasia, can lead to weaker meridional temperature gradients, intensified](#)  
150 [downward solar radiation, reduced cloud cover, and aggravated ozone pollution.](#)  
151 [Atmospheric blocking, a quasi-stationary, large-scale extra-tropical weather system,](#)  
152 [often occurs over expansive regions like the North Atlantic-Europe and North Pacific](#)  
153 [\(Pelly and Hoskins, 2003; Schwierz et al., 2004; Woollings et al., 2018\). Blocking highs](#)  
154 [are frequently associated with extreme weather events \(Barriopedro et al., 2011;](#)  
155 [Cattiaux et al., 2010\). For example, through downstream Rossby wave propagation](#)  
156 [from Alaska to East Asia, Alaska blocking can induce subsequent blocking over the](#)  
157 [Urals, influencing extreme cold events across North America and Eurasia \(Yao et al.,](#)  
158 [2023\)\(Yao et al., 2023\).](#)

159 [Despite significant advancements, the impact of atmospheric blocking on extreme](#)  
160 [weather events and ozone remains insufficiently explored. For example, using a](#)

域代码已更改

161 Hovmöller diagram and local wave activity calculated from 500 hPa geopotential height,  
162 [Sun et al. \(2019\)](#)[Sun et al. \(2019\)](#) found that variations in wave activity can explain 30-  
163 40% of ozone variability in historical U.S. summers. Challenges in global models, such  
164 as simulated biases in atmospheric blocking and ozone, including overestimations  
165 [\(Clifton et al., 2020\)](#)[\(Clifton et al., 2020\)](#), have undermined confidence in linking large-  
166 scale circulation patterns with ozone levels [\(Barnes and Fiore, 2013\)](#).

167 Building on recent advances in high-resolution Earth system models that mitigate  
168 ozone biases [\(Gao et al., in review-b\)](#)[\(Gao et al., in review-b\)](#) and simulate  
169 meteorological parameters and climate extremes (Chang et al., 2020; Gao et al., in  
170 review-a; Gao et al., 2023; Guo et al., 2022), this study is structured as follows. Section  
171 2 describes the model setup. It is followed by an analysis of observational ozone data,  
172 the effects of BVOC emissions, and heatwaves on ozone concentrations. Finally, we  
173 explore how atmospheric blocking influences ozone pollution in eastern China.

174

## 175 **2 Method and data**

### 176 **2.1 Model configurations**

177 In this study, we utilize the Community Earth System Model version 1.3,  
178 employing the Community Atmosphere Model 5.0 (CAM5) as its atmospheric  
179 component. CAM5 runs at two spatial resolutions: nominal  $1^{\circ}$  and  $0.25^{\circ}$ . Sea surface  
180 temperature [\(SST\)](#) and sea ice are prescribed at a spatial resolution of ~~ef~~ $1.0^{\circ} \times 1.0^{\circ}$ .  
181 Atmospheric gas chemistry and aerosol processes are simulated using the Model for  
182 OZone And Related chemical Tracers (MOZART) and the three-mode version of the  
183 Modal Aerosol Module (MAM3). The high-resolution and low-resolution  
184 configurations of CESM are denoted as SW-HRESM and CESM-LR, respectively.  
185 Further details can be found in [Gao et al. \(in review-b\)](#)[Gao et al. \(in review-b\)](#). The  
186 simulation period covers June to August from 2015 to 2019, with May used for spin-up  
187 to mitigate initial condition influences. [Prior to that, a half-year spin-up is applied due](#)  
188 [to the fact that tropospheric ozone initially starts from zero. Specifically, we used a total](#)  
189 [of seven months of spin-up, ensuring that the influence of initial conditions was fully](#)

190 [minimized, thereby guaranteeing the accuracy of the tropospheric ozone simulation.](#)

191 Emissions for the simulations are sourced as follows: anthropogenic emissions  
192 from the Copernicus Atmosphere Monitoring Service global emissions (CAMS-  
193 GLOB-ANT v4.2-R1.1; [Granier et al., 2019](#)),[\(Granier et al., 2019\)](#), with updates for  
194 China based on the Multi-resolution Emission Inventory for China (MEIC; [Li et al.,](#)  
195 [2017](#)),[\(Li et al., 2017\)](#). Volcanic emissions are from Global Emission Inventory  
196 Activity (GEIA), and aircraft emissions from the Community Emission Data System  
197 (CEDS). Biomass burning emissions data are sourced from the Fire INventory from  
198 National Center for Atmospheric Research (FINN) version 2.5 [\(Wiedinmyer et al.,](#)  
199 [2023](#)),[\(Wiedinmyer et al., 2023\)](#). High-resolution simulations use emissions data at 0.1°  
200 resolution, while low-resolution simulations aggregate emissions from 0.1° to ~1.0°  
201 resolution. Biogenic emissions are calculated online using the Model of Emissions of  
202 Gases and Aerosols from Nature version 2.1 (MEGAN2.1; [Guenther et al.,](#)  
203 [2012](#)),[\(Guenther et al., 2012\)](#). Further emission details are available in [Gao et al. \(in](#)  
204 [review-b](#)),[Gao et al. \(in review-b\)](#).

205 Two numerical experiments are designed to assess the impact of BVOC emissions  
206 on ozone. The first experiment includes all emissions (BASE case), while the second  
207 experiment turns off BVOC emissions (No\_BVOC case). By subtracting results from  
208 the No\_BVOC case from those of the BASE case, we isolate the contribution of BVOC  
209 emissions to ozone.

210

## 211 **2.2 Blocking detection method and Rossby wave flux calculation**

212 To identify atmospheric blocking, we use a two-dimensional hybrid blocking index  
213 based on 500 hPa geopotential height. The index is applied across a range of latitudes,  
214  $\phi$ , (40° to 75° N) for each longitude,  $\lambda$ , incorporating meridional gradients to  
215 identify blocked grid points:

$$216 GHGN(\lambda, \phi) = \frac{Z(\lambda, \phi + \Delta) - Z(\lambda, \phi)}{\Delta} < -10 ,$$

217 
$$GHGS(\lambda, \phi) = \frac{Z(\lambda, \phi) - Z(\lambda, \phi - \Delta)}{\Delta} > 0$$
,

218 
$$Z_{\text{anomaly}}(\lambda, \phi) = Z(\lambda, \phi) - \bar{Z}(\phi) > 0,$$

219 where, GHGN (GHGS) indicates the meridional gradient to the north (south) of  
 220 geopotential height at 500 hPa, Z means the 500 hPa geopotential height at longitude  
 221  $\lambda$  along latitude  $\phi$ , and  $\bar{Z}$  is the zonal (0° to 360°) average of Z at latitude  $\phi$ ;  $\Delta$  is  
 222 set as 15°.

223  
 224 A blocking region is defined when the meridional extension of blocked grid points  
 225 exceeds 15°. The center of each blocking region is determined as the grid point with  
 226 maximal 500 hPa geopotential height. Sequential blocking events are identified if the  
 227 center of a blocking region on one day was within a specified distance (27° in latitude  
 228  $\times$  36° in longitude) of the center on the previous day. We restrict a blocking event lasting  
 229 at least five days. More information can be found in [Masato et al. \(2013\)](#)  
 230 [Masato et al. \(2013\)](#) and [Gao et al. \(in review-a\)](#).

域代码已更改

231 To examine Rossby wave propagation, the horizontal stationary wave activity flux  
 232 (W) is calculated following [Takaya and Nakamura \(2001\)](#)  
 233 Key variables used for flux calculation include zonal wind (U), meridional wind (V),  
 234 wind speed ( $|U|$ ), and anomalous geopotential height ( $\Phi'$ ).

235 
$$W = \frac{P \cos \phi}{2|U|} \cdot \left( \frac{U}{a^2 \cos^2 \phi} \left[ \left( \frac{\partial \psi'}{\partial \lambda} \right)^2 - \psi' \frac{\partial^2 \psi'}{\partial \lambda^2} \right] + \frac{V}{a^2 \cos \phi} \left[ \frac{\partial \psi'}{\partial \lambda} \frac{\partial \psi'}{\partial \phi} - \psi' \frac{\partial^2 \psi'}{\partial \lambda \partial \phi} \right] \right. \right. \\ \left. \left. - \frac{U}{a^2 \cos \phi} \left[ \frac{\partial \psi'}{\partial \lambda} \frac{\partial \psi'}{\partial \phi} - \psi' \frac{\partial^2 \psi'}{\partial \lambda \partial \phi} \right] + \frac{V}{a^2} \left[ \left( \frac{\partial \psi'}{\partial \phi} \right)^2 - \psi' \frac{\partial^2 \psi'}{\partial \phi^2} \right] \right) \right), \quad (1)$$

236 where  $W$  represents the wave activity flux (unit:  $\text{m}^2 \text{ s}^{-2}$ ),  $\psi'$  ( $= \Phi'/f$ ) represents the  
 237 geostrophic stream function,  $f$  ( $= 2\Omega \sin \phi$ ) is the Coriolis parameter,  $P$  is the normalized  
 238 pressure (P per 1000 hPa), and  $a$  is Earth's radius.  $\lambda$  and  $\phi$  denote the longitude and  
 239 latitude, respectively.

240

### 241 2.3 Observational data

242 Observational ozone data are collected from several platforms, including the Air

243 Quality System (AQS, <https://www.epa.gov/aqs>; last access: 30 June, 2023) and the  
244 Clean Air Status and Trends Network (CASTNET, <https://www.epa.gov/castnet>; last  
245 access: 30 April, 2023) in the U.S., the European Monitoring and Evaluation  
246 Programme database (EMEP; <http://ebas.nilu.no>; last access: 30 January 2023) in  
247 Europe, and the China National Environmental Monitoring Center (CNEMC,  
248 <http://www.pm25.in>; last access: December 8, 2021) in China. The monitoring network  
249 comprises 1293 sites for AQS, 99 for CASTNET, 286 for EMEP and 2025 for CNEMC.  
250 Meteorological data used in this study are sourced from the National Centers for  
251 Environmental Prediction's Reanalysis-1 (NCEP; [Kalnay et al., 1996](#))([Kalnay et al., 1996](#)).  
252

253

### 254 **3 Results and discussion**

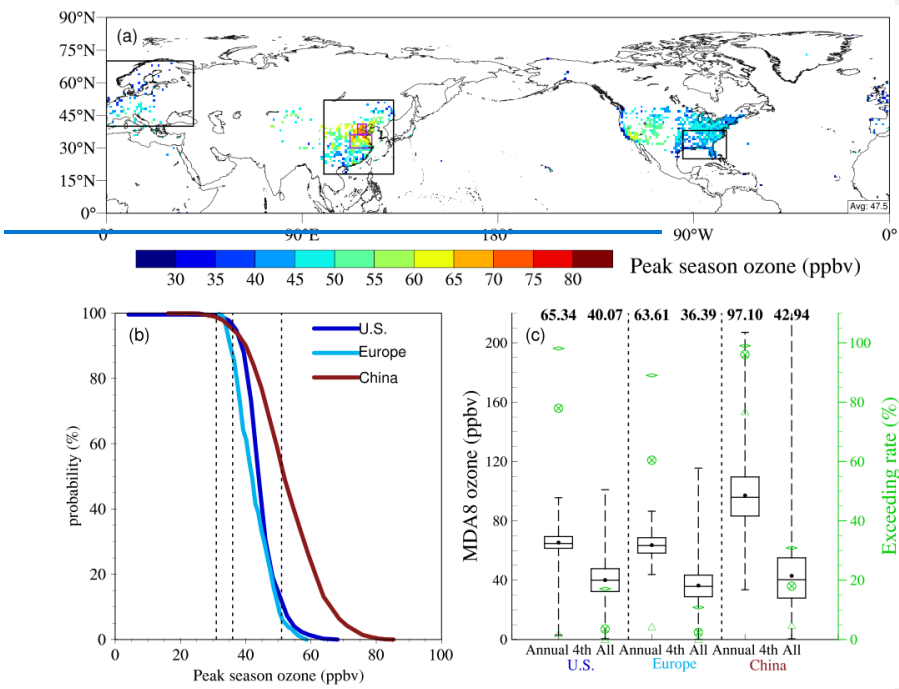
#### 255 **3.1 Characteristics of observed ozone in the Northern Hemisphere**

256 Fig. 1 illustrates the characteristics of observed ozone levels based on a  
257 comprehensive analysis of extensive observational datasets,[with ozone exceedance](#)  
258 [rates shown in Table 1](#). Peak season ozone (Fig. 1a), as defined by the WHO in 2021,  
259 is determined using a 6-month running average of maximum daily 8-h ([MDA8](#))-ozone  
260 concentrations for each grid, with the maximum value being considered. The WHO air  
261 quality guideline is set at  $60 \mu\text{g}\cdot\text{m}^{-3}$  (31 ppbv; [level II](#)), with additional standards of  $100$   
262  $\mu\text{g}\cdot\text{m}^{-3}$  (51 ppbv; [level I](#)) and  $70 \mu\text{g}\cdot\text{m}^{-3}$  (36 ppbv; [Air Quality Guideline](#)). Regional  
263 differences in ozone pollution are apparent: higher concentrations are observed in the  
264 western U.S. due to elevated altitude and background levels ([Parrish et al., 2021a](#)). Specific sites with significant ozone pollution include  
265 [L.A. and Houston, as previously documented \(Dunker et al., 2017\)](#)[Los Angeles and](#)  
266 [Houston, as previously documented \(Dunker et al., 2017\)](#). In Europe, ozone pollution  
267 is more pronounced in southern regions, particularly around the Mediterranean,  
268 consistent with earlier studies (Zohdirad et al., 2022). In China, the eastern region  
269 exhibits concentrated pollution. Mean peak season ozone levels are 45.5 ppbv in the  
270 U.S., 42.9 ppbv in Europe, and 53.7 ppbv in China.  
271

272 The cumulative distribution function of peak season ozone concentrations is  
273 shown in Fig. 1b using gridded data. In the U.S. and Europe, only 15% and 8% of the  
274 peak season ozone concentrations, respectively, exceed the level I ([51 ppbv](#)[51 ppbv](#))  
275 from 2015 to 2019, whereas in China, almost 60% exceed this threshold. However,  
276 when applying the stricter standard ([36 ppbv](#)[36 ppbv](#)), exceedance rates are notably high:  
277 98%, 89%, and 96% in the U.S., Europe and China, respectively.

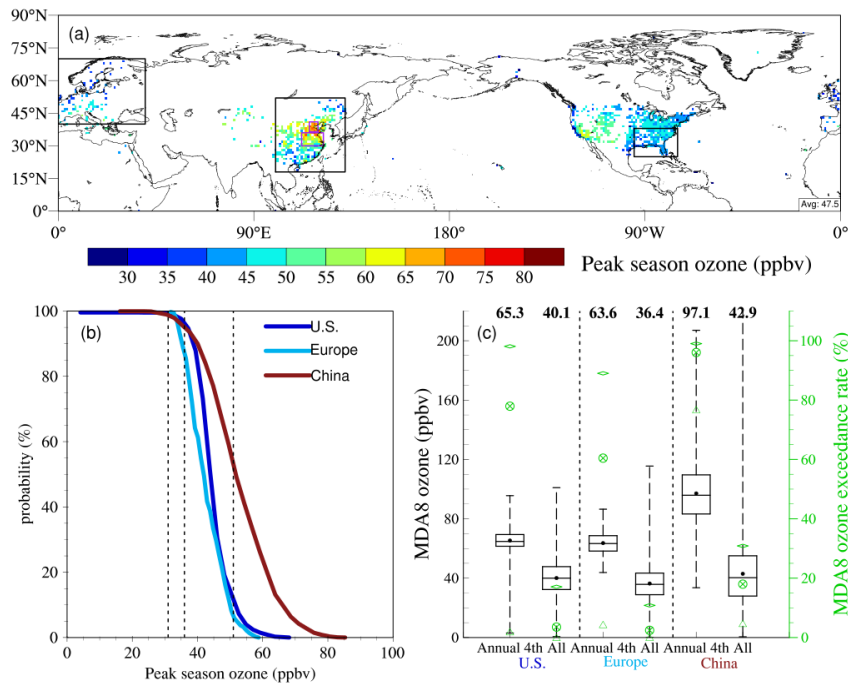
278 Fig. 1c presents the fourth highest MDA8 ozone values annually from 2015 to  
279 2019, alongside daily values for the U.S., Europe and China. The WHO has established  
280 standards at 82 ppbv and 61 ppbv, with an air quality guideline of [51 ppbv](#)[51 ppbv](#).  
281 Exceedance rates ([Table 1](#)) for the strictest guideline (51 ppbv) are 98%, 89% and 99%  
282 in the U.S., Europe and China, respectively. [For the 61 ppbv standard, rates are 78%,](#)  
283 [60% and 96%, respectively, and for the 82 ppbv standard, exceedance rates are 2%, 4%](#)  
284 [and 77%, respectively.](#) Considering all daily values, with a sample size approximately  
285 365 times larger than the annual fourth highest value, the rates of ozone exceedance  
286 (i.e., exceeding 51 ppbv) are observed to be 17% in the U.S., 11% in Europe, and 31%  
287 in China. This indicates that there are significantly more days where ozone levels  
288 exceed the threshold beyond just the fourth highest maximum daily 8-hour ([MDA8](#))  
289 ozone level in these regions. This suggests that air quality issues related to ozone are  
290 more persistent and widespread than what might be inferred solely from the fourth  
291 highest MDA8 metric.

292



293

294



295  
296 **Fig. 1 Peak season ozone concentrations and maximum daily 8-hr (MDA8)-ozone**  
297 **concentrations.** (a) Spatial distribution of mean peak season ozone concentrations in  
298 the Northern Hemisphere from 2015 to 2019. The black squares represent regions in  
299 Europe, eastern China, and the U.S., while the purple squares in eastern China denote  
300 North China and central eastern China regions. (b) Cumulative Distribution Function  
301 of peak season ozone concentrations, with dashed lines indicating WHO standard  
302 values (31 ppbv, 36 ppbv, 51 ppbv) set by WHO. (c) Box-and-whisker plot of annual  
303 fourth-highest (left) and all (right) MDA8 ozone during 2015-2019 in the U.S., Europe  
304 and China. The boxes represent the interquartile range (25th to 75th percentiles),  
305 horizontal lines denote medians, solid points indicate averages, and line end points  
306 show maximum and minimum values, with the averages shown on top of each box.  
307 Exceedance rates (%) of MDA8 ozone to WHO standards of 82 ppbv, 61 ppbv, and 51  
308 ppbv are marked with green triangle, crossed-out circle, and diamond symbols,  
309 respectively.

310 ▲ 设置了格式: 字体: 非加粗

311 **Table 1. Regional mean ozone exceedance rates (%) during 2015-2019**

Region	Annual 4th			All days		Peak season	
	51 ppbv	61 ppbv	82 ppbv	51 ppbv	61 ppbv	36 ppbv	51 ppbv
U.S.	98	78	2	17	4	98	15
Europe	89	60	4	11	2	89	8
China	99	96	77	31	18	96	60

312

313 **3.2 BVOC emissions and their effects on ozone**

314 BVOC emissions during the summer months of 2015-2019 are depicted in Fig. 2a  
 315 and Fig. 2b, with global totals of 86.0 Tg month<sup>-1</sup> in SW-HRESM and 90.7 Tg month<sup>-1</sup>  
 316 in CESM-LR. Isoprene emissions (Fig. 2c, d) account for nearly half of these totals  
 317 amounting to 42.3 Tg month<sup>-1</sup> in SW-HRESM and 45.2 Tg month<sup>-1</sup> in CESM-LR. This  
 318 predominance of isoprene emissions aligns with previous studies (Ma et al., 2022;  
 319 Mochizuki et al., 2020). Isoprene emissions are predominantly concentrated in tropical  
 320 regions, reflecting the prevalence of dense forest cover. Our study indicates values  
 321 approximately 30% higher than those (Fig. S1) reported in [Weng et al. \(2020\)](#)  
 322 [al. \(2020\)](#) due to previously underestimated emissions in tropical regions.

323 To assess the utility of high-resolution simulations, we compute the standard  
 324 deviation across 16 grid points in SW-HRESM corresponding to a single low-resolution  
 325 grid (Fig. S2). The average monthly isoprene emissions during 2015-2019 are 0.63 kg  
 326 m<sup>-2</sup>, 0.51 kg m<sup>-2</sup> and 0.21 kg m<sup>-2</sup> over the U.S., Europe and China (Fig. 2c), respectively,  
 327 with mean standard deviation of 0.13 kg m<sup>-2</sup>, 0.11 kg m<sup>-2</sup>, 0.05 kg m<sup>-2</sup> (Fig. S2). This  
 328 ratio also applies to biogenic emission-rich areas such as the southeastern U.S., southern  
 329 Europe and eastern China, highlighting the importance of using finer grid spacings for  
 330 accurately capturing the spatial heterogeneity of BVOC emissions.

331 The spatial distribution of BVOC emissions closely correlates with the distribution  
 332 of broadleaf trees (Fig. S3), which have higher emission factors compared to other plant  
 333 types (Table 2 in Guenther et al., 2012). S3, which have higher emission factors  
 334 compared to other plant types (Table 2 in (Guenther et al., 2012)). Isoprene emissions  
 335 are most intense in tropical regions where broadleaf evergreen and deciduous tropical

336 trees predominate, as well as in mid-to-high latitude belts and isolated hotspots in mid-  
337 latitudes like the southeastern U.S., southern Europe, and eastern China.

338 An exception is observed in the Amazon region, where despite dense broad  
339 evergreen tropical forest cover, the largest isoprene and BVOC emissions occur away  
340 from the main forest area. This Amazon hotspot, noted in previous studies ([Opacka et](#)  
341 [al., 2021](#))[\(Opacka et al., 2021\)](#), is influenced by key meteorological factors such as 2-  
342 meter air temperature and downward surface solar radiation (Fig. S4). Specifically,  
343 areas with higher temperatures and stronger solar radiation exhibit greater BVOC and  
344 isoprene emissions. The discrepancy in temperature between CESM-LR and SW-  
345 HRESM simulations reveals nuances in emission patterns, with CESM-LR showing  
346 slightly higher temperatures that lead to increased emissions. The slightly lower  
347 temperature in higher grid spacing simulations in regional climate model was also  
348 reported by [Pugh et al. \(2013\)](#)[\(Pugh et al. \(2013\)\)](#). They suggested that improved  
349 representation of forests could increase latent heat flux and thereby mitigate  
350 temperature rises through a reduced sensible heat. The study compared three grid  
351 spacings: 0.1°, 0.5°, and 2.0°, showing that across regions such as South America,  
352 Southeast Asia, and the southeastern U.S., there was a small overall difference of about  
353 2% in BVOC emissions on a regional scale. However, this difference could reach up to  
354 150% in high-emission areas.

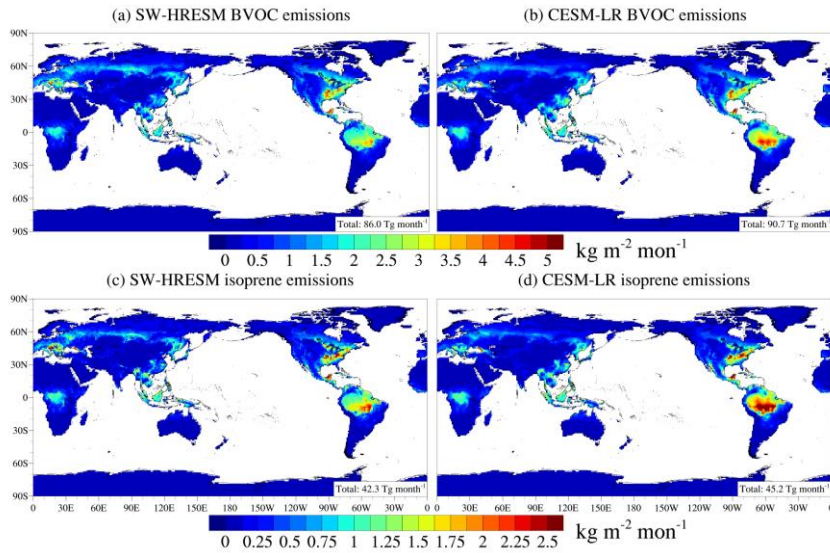


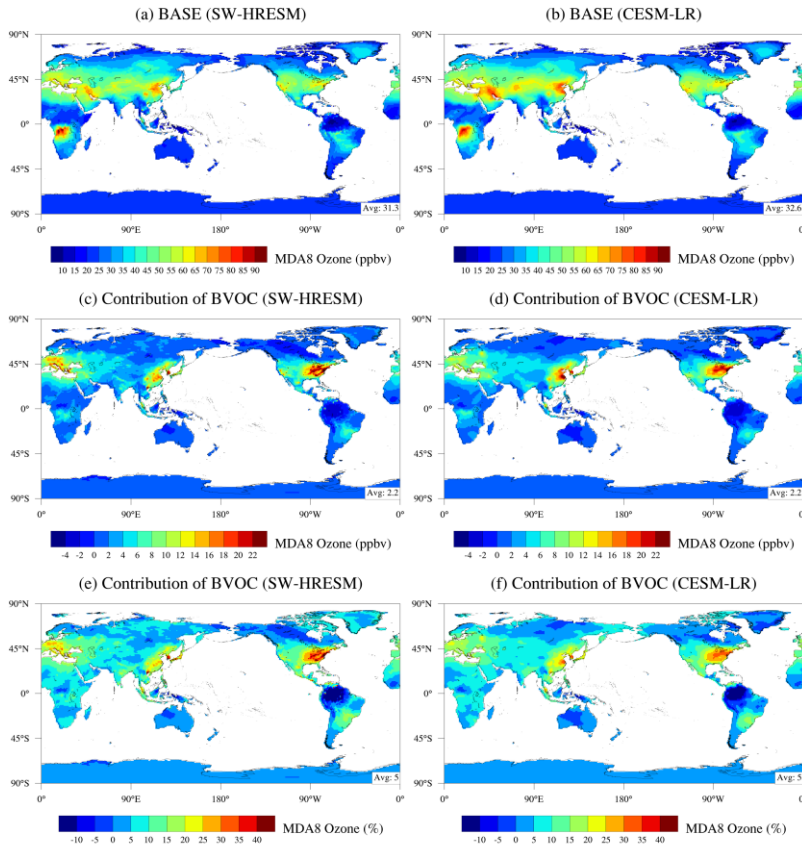
**Fig. 2 Spatial distribution of BVOC (top) and isoprene (bottom) emissions based on SW-HRESM (left) and CESM-LR (right).** Shown are monthly total emissions averaged during the summer of 2015-2019.

To understand the contribution of BVOC emissions to ozone concentrations across different grid resolutions, we compare two scenarios: one with biogenic emissions included and one without. Fig. 3a and 3b illustrate the spatial distribution of ozone concentrations averaged over the summers of 2015-2019 for both SW-HRESM and CESM-LR. Both models identify significant ozone pollution areas in the Northern Hemisphere, particularly over southern Europe, the southeastern U.S., and eastern China. The contribution of BVOC emissions to ozone concentrations is further detailed in Fig. 3c-f.

In SW-HRESM, BVOC emissions contribute approximately 2.2 ppbv to the global mean ozone concentrations over land, representing 7% relative to the mean value of 31.3 ppbv (Fig. 3c,e). However, the impact of BVOC emissions on ozone concentrations is modulated by factors such as anthropogenic emissions and meteorological conditions. Regions with abundant BVOC emissions and higher ozone

373 concentrations, such as the U.S., Europe, and eastern China, show a substantial  
374 contribution of 15% to 30% from BVOC emissions to ozone levels. In contrast, the  
375 Amazon rainforest in Brazil, despite having the highest BVOC emissions, exhibits a  
376 negative contribution to ozone levels. This is attributed to the fact that in regions with  
377 low NO<sub>x</sub> concentrations, increased VOCs initiated by OH oxidation can lead to the  
378 formation of stable organic nitrogen compounds, through increasing organic peroxy  
379 radicals and elevating the reaction with NO<sub>2</sub> ([Tonnesen and Jeffries, 1994](#)) ([Tonnesen](#)  
380 [and Jeffries, 1994](#)). It reduces the availability of NO<sub>2</sub> and the subsequent photolysis  
381 such as a reduction of O<sub>3</sub>P, thereby reducing ozone concentrations (Kang et al., 2003;  
382 Unger, 2014). While this effect is evident in CESM-LR, lower resolution simulations  
383 may overlook finer-scale variability, affecting the accuracy of quantifying the impact  
384 of BVOC emissions on ozone.

385  
386



387

388 **Fig. 3 Spatial distribution of MDA8 ozone from SW-HRESM (left) and CESM-LR**  
 389 **(right).** Shown are results of ozone concentrations at BASE (top)  
 390 and the contribution  
 391 of BVOC emissions to ozone (middle row: ppbv; bottom row: %). Global mean values  
 392 over land are indicated in the bottom right.

393

### 3.3 Effects of heatwaves on ozone

394 Heatwaves not only accelerate photochemical reactions but also intensify BVOC  
 395 emissions, thereby amplifying ozone production and exacerbating ozone pollution.  
 396 Building on previous studies (Gao et al., 2012; Sillmann et al., 2013), heatwaves are  
 397 defined within each grid as periods when the daily mean near-surface air temperature  
 398 exceeds the 90th percentile of the climatological mean, focusing on the summer period

399 from 2015 to 2019 in this study. To quantify the impact of heatwaves on ozone  
400 concentrations, Fig. 4 illustrates the probability distribution function (PDF) of MDA8  
401 ozone concentrations for both the BASE case and a scenario without BVOC emissions,  
402 aggregated across entire summer periods and specifically during heatwave days. Given  
403 the superior capability of high-resolution simulations in reproducing heatwaves and  
404 ozone concentrations (Gao et al., in review-b; Gao et al., 2023), we present results  
405 solely from SW-HRESM hereafter.

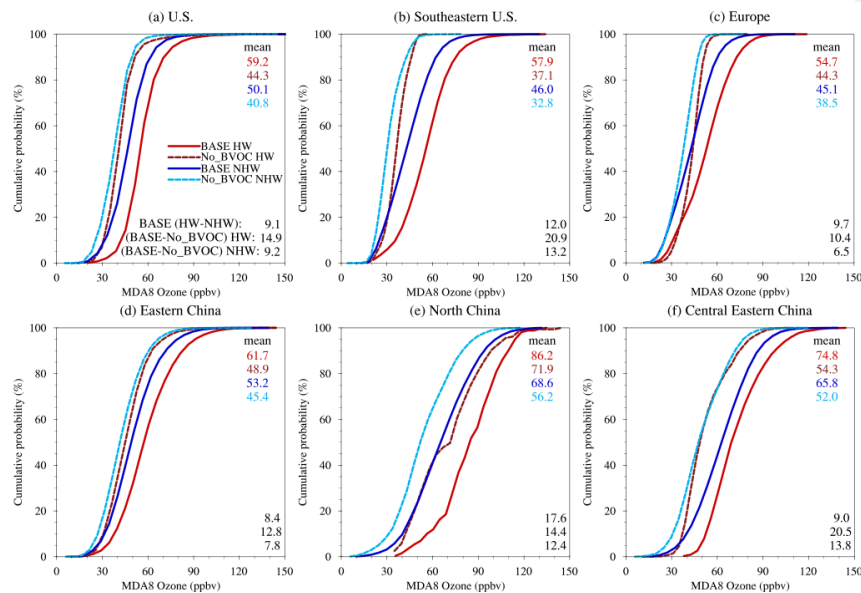
406 Several notable observations emerge. Firstly, a comparison of heatwave periods to  
407 non-heatwave periods (solid red vs. solid blue lines in Fig. 4) reveals a noticeable  
408 rightward shift in the PDF, indicating an increase in ozone levels due to heatwave  
409 impacts, a well-established phenomenon (e.g., (Gao et al., 2020; Zhang et al., 2018)).  
410 Specifically, compared to non-heatwave periods, mean ozone concentrations increase  
411 by 9.1 ppbv, 9.7 ppbv, and 8.4 ppbv during heatwaves over the U.S., Europe, and eastern  
412 China, respectively. This effect is more pronounced in specific regions, such as North  
413 China (NC) with an increase of 17.6 ppbv, followed by the southeastern U.S. (12.0 ppbv)  
414 and central eastern China (CECN) (9.0 ppbv), accounting for 12% to 21% of regional  
415 mean ozone levels. A previous study noted that median-surface ozone concentrations  
416 during U.S. heatwaves from 1990 to 2016 could increase by 10% to 80% (Meehl et al.,  
417 2018)(Meehl et al., 2018).

418 Comparing scenarios with and without BVOC emissions (solid vs. dashed lines in  
419 Fig. 4), BVOC emissions significantly contribute to ozone enhancement during both  
420 non-heatwave and heatwave periods. For instance, during heatwaves, BVOC emissions  
421 contribute 20.9 ppbv, 10.4 ppbv, 14.4 ppbv, and 20.5 ppbv over the southeastern U.S.,  
422 Europe, North China, and central eastern China, respectively. A study by Churkina et  
423 al. (2017) found that biogenic emissions contributed 17-20% to ozone formation in  
424 Berlin, Germany, in July 2006, with this contribution potentially increasing to 60%  
425 during heatwaves.

426 It is important to note that the influence of BVOC emissions persists outside of  
427 heatwave periods, particularly when downward surface solar radiation remains

428 sufficiently high (Fig. S5). The differences in BVOC contributions to ozone between  
 429 heatwave and non-heatwave periods represent the incremental effect of BVOCs during  
 430 heatwaves, accounting for 7.7 ppbv, 3.9 ppbv, 2.0 ppbv, and 6.7 ppbv over these four  
 431 regions, respectively. This incremental effect constitutes 64%, 40%, 11%, and 74% of  
 432 the total heatwave effects, indicating varying degrees of BVOC influence across  
 433 different regions. The relatively smaller incremental BVOC effect during heatwaves  
 434 over North China is partly attributed to higher anthropogenic emissions and lower  
 435 BVOC emissions compared to the other regions. With potential reductions in  
 436 anthropogenic emissions in China, BVOC emissions could assume a more pivotal role,  
 437 especially given projections of increased frequency of heatwaves in a warming climate  
 438 (Gao et al., 2023; Gao et al., 2022).

439



440  
 441 **Fig. 4 Cumulative Density Function (CDF) of MDA8 ozone concentrations.** Shown  
 442 are results for the BASE case (solid line) and the case without BVOC emissions (dashed  
 443 line), during heatwaves (red) and non-heatwaves (blue) based on SW-HRESM.

444

445

446 **3.4 The role of atmospheric blocking on ozone pollution in eastern China**

447 Eastern China has emerged as a significant region grappling with severe ozone  
448 pollution. Numerous studies have endeavored to explore the driving factors,  
449 particularly in the last decade, leveraging the widespread availability of ozone data  
450 across China. For example, through the examination of ozone pollution events in North  
451 China during 2014-2017, [Gong and Liao \(2019\)](#)[Gong and Liao \(2019\)](#) investigated  
452 ozone pollution episodes in North China from 2014 to 2017 and identified that under  
453 weather conditions characterized by high near-surface air temperatures, low relative  
454 humidity, and anomalous southerly winds in the lower troposphere, ozone  
455 concentrations tend to accumulate in this region. [Mousavinezhad et al. \(2021\)](#)[Mousavinezhad et al. \(2021\)](#) utilized a multiple linear regression model to  
456 disentangle the contributions of meteorology and emissions to ozone levels in North  
457 China during 2015-2019. Their findings indicated that meteorological factors such as  
458 increased downward surface solar radiation and near-surface air temperatures  
459 accounted for 32% of the observed ozone increase, while changes in emission  
460 precursors contributed 68%. To elucidate the interannual variability of ozone in North  
461 China, [Gong et al. \(2020\)](#)[Gong et al. \(2020\)](#) employed tagged O<sub>3</sub> simulations with the  
462 Goddard Earth Observing System Chemical Transport Model (GEOS-Chem) model  
463 and suggested that one-third of the rise in ozone pollution days observed from 2014 to  
464 2018, particularly in 2018, could be attributed to emissions transport from central-  
465 eastern China. Considering the intertwined roles of meteorology and emissions, the  
466 focus shifted to examining ozone anomalies relative to their respective monthly  
467 averages, thereby minimizing the influence of emissions on ozone variability.

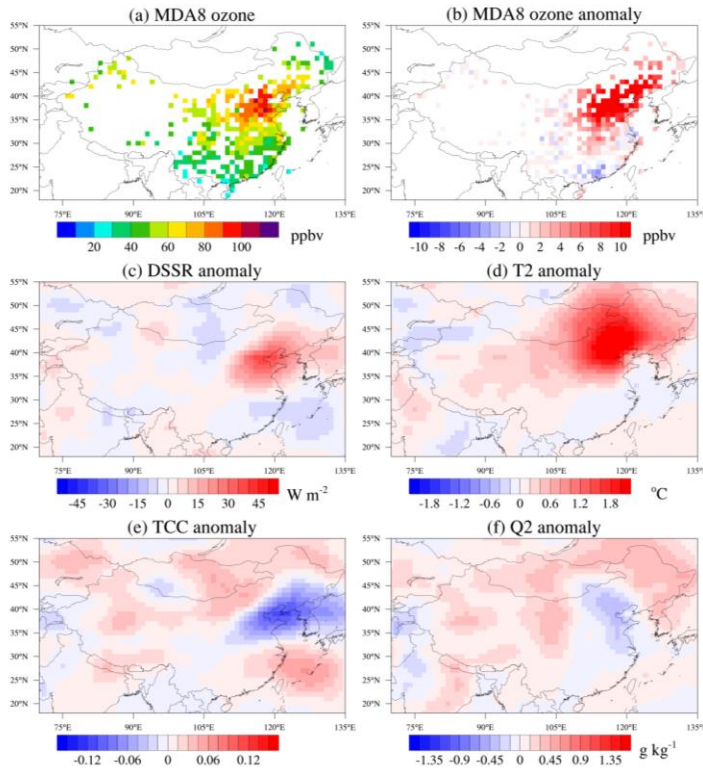
468 The study focuses on two specific regions—North China and central eastern  
469 China—to analyze days where regional mean MDA8 ozone levels exceeded 10 ppbv  
470 of their respective monthly means, defined as regional ozone pollution events.  
471 Observational data indicate a total of 131 and 89 such events in North China and central  
472 eastern China, respectively, during the summers of 2015-2019. Ozone pollution events  
473 are observed to extend meridionally (Figs. 5,6), northward into northeastern China from

475 North China (Fig. 5a,b) and covering large areas of northern and southern China from  
476 central eastern China (Fig. 6a,b).

477

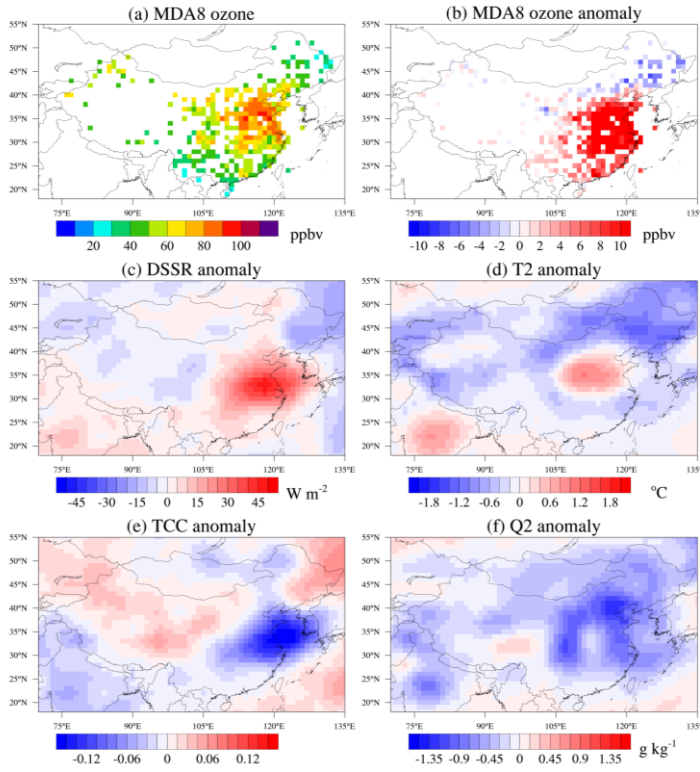
478 During regional ozone pollution events, concurrent meteorological conditions  
479 typically feature higher downward surface solar radiation, 2-meter air temperatures,  
480 reduced water vapor, and decreased total cloud cover, all of which favored ozone  
481 accumulation. Meteorological anomalies for each day are computed relative to their  
482 respective months, with the study testing four different methods for deriving  
483 climatology, including averages from the same day, same month, summer periods from  
484 2015-2019, and summers from 1990-2019. They all yield comparable results.  
485 Analyzing atmospheric blocking, we find that 43% (56 events) of regional ozone  
486 pollution events in North China and 48% (43 events) in central eastern China are  
487 accompanied by blocking. Notably, among the 36 events where ozone pollution  
488 concurrently affected both North China and central eastern China, nearly 40% are  
489 associated with blocking events.

490



491

492 **Fig. 5 Spatial distributions of ozone and meteorological conditions during ozone  
 493 pollution events in North China.** Shown are composited results of (a) mean MDA8  
 494 ozone concentrations, anomalies of (b) MDA8 ozone, (c) downward surface solar  
 495 radiation, (d) 2-m air temperature, (e) total cloud cover, and (f) 2-m specific humidity  
 496 during the summers of 2015-2019.  
 497



498

499 **Fig. 6 Spatial distributions of ozone and meteorological conditions during ozone**  
500 **pollution events in central eastern China.** Shown are composited results of (a) mean  
501 MDA8 ozone concentrations, anomalies of (b) MDA8 ozone, (c) downward surface  
502 solar radiation, (d) 2-m air temperature, (e) total cloud cover, and (f) 2-m specific  
503 humidity during the summers of 2015-2019.

504

505

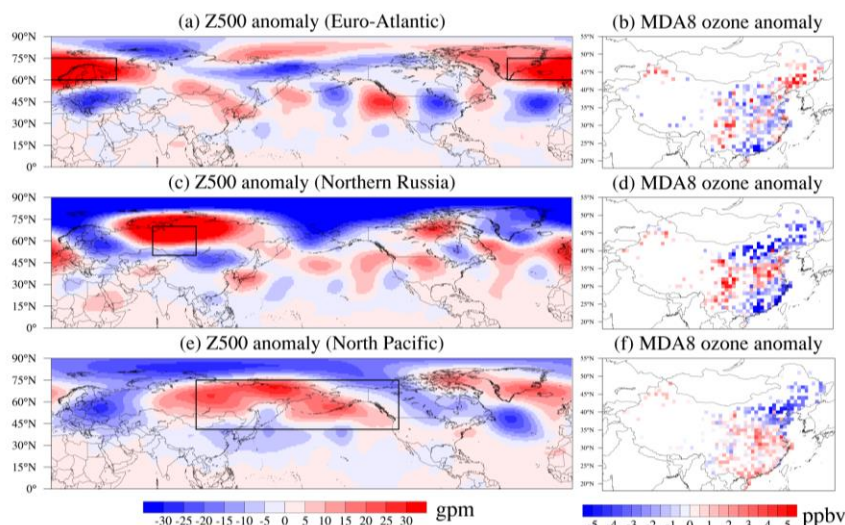
506 The impact of blocking events on downstream meteorological conditions and ozone  
507 pollution is examined, primarily based on Rossby wave propagation, which profoundly  
508 affects large-scale circulations. For example, [Ding and Li \(2017\)](#) [Ding and Li \(2017\)](#)  
509 analyzed reanalysis data from 1951–2015 and found that Rossby waves originating  
510 from northwest Europe entered the North Africa-Asia westerly jet in the upper  
511 troposphere, propagating eastward along the subtropical westerly jet. This circulation

512 favored persistent heavy rainfall events in South China (20°–30°N). [Liu et al. \(2022\)](#)  
513 [Liu et al. \(2022\)](#) studied data from 1979–2020 and observed positive anomalies in summer  
514 shortwave cloud radiative effects over northern Russia, promoting the generation of  
515 Ural blocking. This blocking dynamically triggered a positive Eurasian pattern  
516 characterized by a “+ – +” wave train, resulting in positive precipitation anomalies in  
517 northern China and strong heatwaves in southern China. In addition to northwest  
518 Europe and northern Russia, blocking also occurs over northeastern Russia. This,  
519 combined with the land-sea temperature contrast between warm northeastern Eurasia  
520 and the colder Oyashio region in the North Pacific, may induce a north–south-tilting  
521 anticyclone, leading to increased temperatures across a wide area of China [\(Amano et](#)  
522 [al., 2023\)](#)[\(Amano et al., 2023\)](#).

523 Blocking events are categorized into Euro-Atlantic, northern Russia, and North  
524 Pacific regions (Fig. 7), based on their geographical locations. Analysis of NCEP  
525 reanalysis data during the summers of 2015–2019 identified a total of 227 blocking days  
526 in the Northern Hemisphere, with approximately 50% occurrence. Of these, 60 days  
527 occurred over the Euro-Atlantic sector, 68 days over northern Russia, and 162 days over  
528 the North Pacific. The higher frequency of blocking in the North Pacific is partly due  
529 to conducive conditions in northeastern Russia and Alaska. Notably, the sum of  
530 blocking events across these regions exceeds the total for the Northern Hemisphere,  
531 owing to concurrent events in multiple areas. [High blocking frequency has previously](#)  
532 [been reported \(Lupo, 2021\)](#)[High blocking frequency has previously been reported](#)  
533 [\(Lupo, 2021\)](#), indicating climatologically in the Northern Hemisphere there are 30–35  
534 blocking events per year with a mean duration of 9 days. This occurrence rate is higher  
535 than in our study, partly due to the larger frequency in winter and fall compared to  
536 summer.

537 Anomalies of 500 hPa geopotential height from reanalysis data and MDA8 ozone  
538 from observations during composite blocking events over Euro-Atlantic, northern  
539 Russia, and North Pacific are depicted in Fig. 7. These illustrations highlight the  
540 characteristics of Rossby wave propagation and the corresponding variations in ozone.

541 For instance, when blocking occurs over the Euro-Atlantic (top of Fig. 7), it coincides  
 542 with anomalously high pressure, triggering a wave number of 5 and resulting in high  
 543 pressure over northern China. This configuration leads to high ozone anomalies over  
 544 northeastern China, with scattered spots of high ozone anomalies over parts of North  
 545 China and central eastern China. When blocking shifts eastward to northern Russia  
 546 (middle row in Fig. 7), a positive Eurasian pattern emerges with a “+ – +” wave train.  
 547 This pattern manifests in negative anomalies in the northern flank of China and positive  
 548 pressure anomalies in central to southern eastern China, South Korea, and southern  
 549 Japan. During blocking over the North Pacific, spanning northeastern Russia and  
 550 Alaska (Fig. 7e), broad positive anomalies are observed in southern China. However,  
 551 notable anomalies of 500 hPa geopotential height are absent in southern China, and  
 552 positive high pressure is not always accompanied during ozone pollution events (Yang  
 553 et al., 2024)(Yang et al., 2024).



554  
 555 **Fig. 7 Spatial distributions of anomalies in 500 hPa geopotential height (gpm) and**  
 556 **ozone.** Shown are composited results during blocking events over Euro-Atlantic sector  
 557 (top), northern Russia (middle), and the North Pacific (bottom), indicated by the black  
 558 square.

559

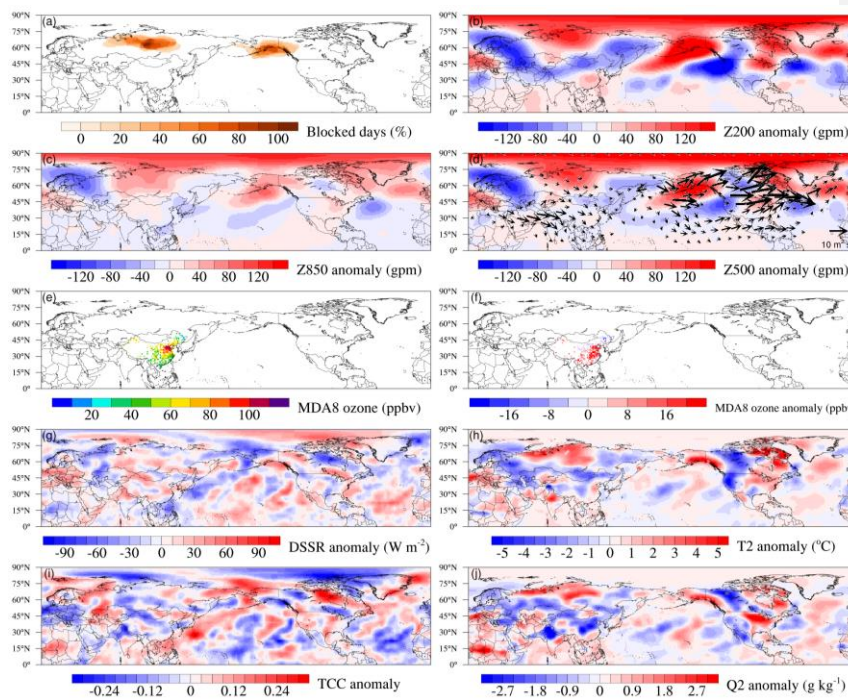
560 To further elucidate the pathway of Rossby wave propagation, we focus on a typical  
561 blocking event from June 27 to July 4, 2019. During this period, a blocking high is  
562 situated over northern Russia and the eastern flank of the Ural Mountains (Fig. 8a).  
563 Coincidentally, another blocking event (June 29 - July 4, 2019) occurs over the North  
564 Pacific near Alaska. regions with convergence of wave activity flux indicate weakened  
565 westerlies, suggesting an incoming wave train and accumulation of wave activity in  
566 these areas. This accumulation could further amplify the blocking high (Nakamura et  
567 al., 1997; Schneidereit et al., 2012), serving as a source region for Rossby wave  
568 propagation.

569 A strong high-pressure system over northern Russia (Fig. 8a), propagating  
570 southeastward (arrows in Fig. 8d). This propagation stimulates positive height  
571 anomalies over central eastern China, evident in both the upper (200 hPa; Fig. 8b) and  
572 mid-troposphere (500 hPa; Fig. 8d), with a weaker signal observed at the lower  
573 troposphere (850 hPa; Fig. 8c), indicating a barotropic structure (Barriopedro et al.,  
574 2006; Sui et al., 2022). The blocking events over northern Russia may originate from  
575 the North Atlantic, as indicated by [\(Liu et al., 2022\)](#)[\(Liu et al., 2022\)](#). This is suggested  
576 by the presence of a positive geopotential height anomaly over the northern North  
577 Atlantic, which then propagates northeastward towards northern Europe and Russia.  
578 This pattern resembles the Rossby wave train with a zonal wavenumber of 5, as  
579 described in [\(Xu et al. \(2019\)\)](#)[\(Xu et al. \(2019\)\)](#). It originates west of the British Isles and  
580 propagates towards Lake Baikal, simulating a high-pressure system on the southern  
581 flank of China. The blocking over Alaska serves as another source of Rossby waves,  
582 propagating eastward towards the Atlantic and triggering another pathway through the  
583 Mediterranean Sea along the subtropical jet. This process further enhances high-  
584 pressure anomalies over central eastern China (Fig. 8d).

585 Modulated by this large-scale circulation, there is an increase in downward surface  
586 solar radiation, 2-m air temperature, reduced water vapor, and total cloud cover over  
587 areas spanning 25° to 40°N (Fig. 8g-j). These conditions contribute to widespread  
588 ozone increases in this region, extending slightly into North China and southern China

589 (Fig. 8e,f). Comparably, when atmospheric blocking occurs over Euro-Atlantic region,  
 590 a Rossby wave propagates southeastward from the northern Atlantic. This triggers high  
 591 pressure anomalies in North China and central eastern China, creating meteorological  
 592 conditions that favor anomalously high ozone concentrations (July 20 - 24, 2017, Fig.  
 593 S6). Additionally, a concurrent blocking event over the North Pacific initiates another  
 594 Rossby wave propagation, which converges with the Rossby wave originating from the  
 595 Euro-Atlantic blocking. This convergence reinforces the eastward propagation of the  
 596 Rossby wave.

597



598 **Fig. 8 Spatial distribution of blocking, ozone and geopotential height.** Shown are  
 599 results of anomalies of geopotential height at (b), 200 hPa, (c) 850 hPa, (d) 500 hPa, (e)  
 600 ozone concentrations, anomalies of (f) ozone, (g), DSSR, (h) 2-m air temperature, (i)  
 601 total cloud cover and (j) 2-m specific humidity. The results are composited during a  
 602 specific blocking event over northern Russia.

604

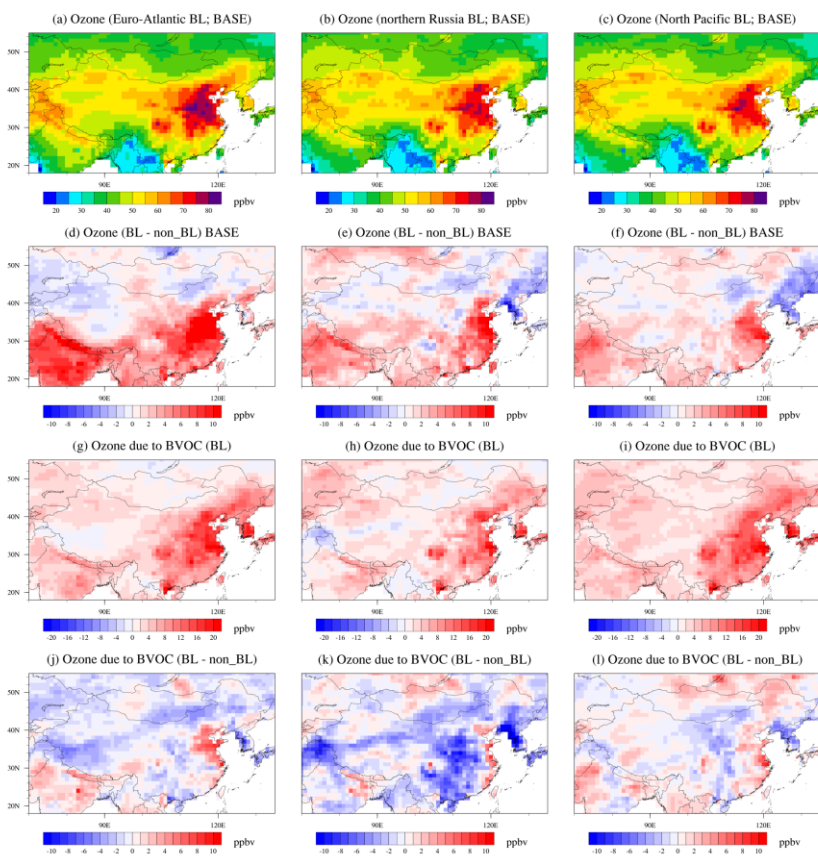
605 Next, we explore how atmospheric blocking influences ozone through the effect of  
606 BVOC emissions. In a previous study, significant improvements in summer blocking  
607 simulations were achieved by increasing horizontal resolution in an Earth system model  
608 with coupled atmosphere and ocean components ([Gao et al., in review-a](#)) ([Gao et al., in](#)  
609 [review-a](#)). Driven by the prescribed SST, high-resolution simulations have shown  
610 enhanced blocking frequencies, particularly over the Ural Mountains and North Pacific  
611 (Fig. S7). Therefore, the analysis below is based solely on SW-HRESM.

612 We composite blocking events occurring over the Euro-Atlantic sector (100 days),  
613 northern Russia (47 days) and North Pacific (119 days), and the spatial distribution of  
614 ozone concentrations is shown in Fig. 9. The probability distribution function of ozone  
615 concentrations is shown in Fig. 10. Several distinctive features emerge. During non-  
616 blocking periods (Fig. S8a; Fig. 10), the mean ozone concentrations over North China  
617 is slightly higher (66.3 ppbv) than in central eastern China (63.3 ppbv). Among all three  
618 blocking categories, ozone concentrations over central eastern China tend to increase  
619 to a larger extent compared to North China, resulting in comparable or higher ozone  
620 concentration in central eastern China relative to North China (Fig. 9d,e,f). Specifically,  
621 blocking triggers an ozone increases of 10.7 ppbv, 7.1 ppbv and 5.9 ppbv when blocking  
622 occurs in the Euro-Atlantic, northern Russia and North Pacific sectors, respectively,  
623 compared to values of 4.9 ppbv, 4.2 ppbv and 2.1 ppbv in North China (Fig. 10). When  
624 blocking occurs in northern Russia and the North Pacific, the effect can extend further  
625 south from central to southeastern China. Accompanied by the blocking, an increase in  
626 downward surface solar radiation, 2-m air temperature, along with reduced water vapor,  
627 and total cloud cover, emerges primarily over North China and central eastern China  
628 (Fig. S9). Despite slight differences, this feature is consistent with the observed patterns  
629 (Fig. 7b,d,f).

630 BVOC emissions play important roles in modulating ozone concentrations. When  
631 the blocking occurs, the effects of BVOC emissions on ozone concentrations range  
632 from 10.6 ppbv to 15.5 ppbv over North China and central eastern China (Fig. 9g,h,i;  
633 Fig. 10), with the largest effect when blocking occurs over the Euro-Atlantic sector.

634 Consistent with the previous discussion on heatwaves (section 3.3), BVOC emissions  
 635 play a role even in the absence of blocking (Fig. S8b), with effects of 10.8 ppbv over  
 636 North China and 13.3 ppbv over central eastern China. The effect of BVOC emission  
 637 on ozone during blocking is larger than during non-blocking for most cases, except over  
 638 central eastern China during blocking in northern Russia, which is visible when  
 639 blocking is compared to a lower temperature range (i.e.,  $< 26^{\circ}\text{C}$ ; Fig. S10). Overall, the  
 640 incremental effect of BVOC emissions on ozone during blocking, similar to that defined  
 641 in section 3.3, is calculated, and it could reach account for as much as 65% of the ozone  
 642 increase during blocking in North China 31% of the ozone increase during blocking in  
 643 central eastern China (Fig. 9j,k,l vs. Fig. 9g,h,i; Fig. 10).

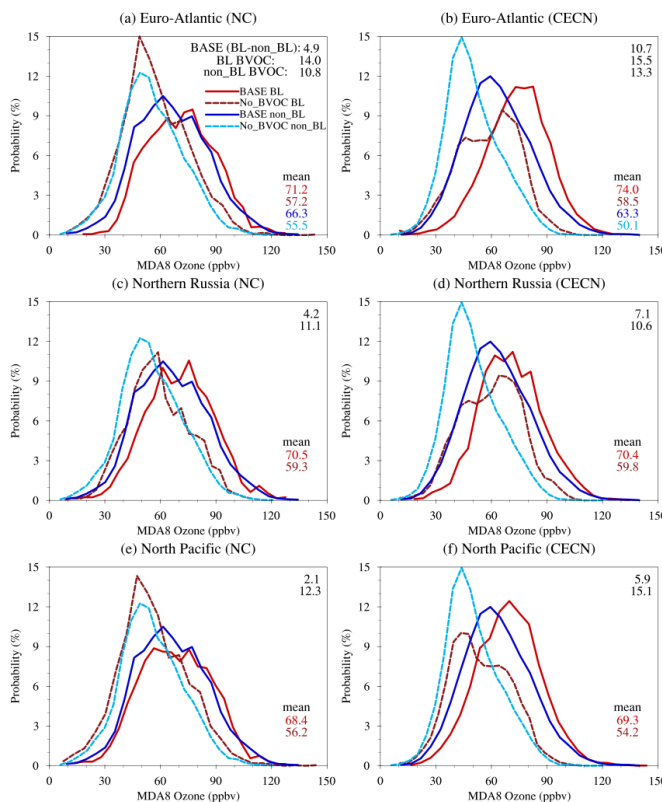
644



645

646 **Fig. 9 Spatial distributions of ozone concentrations.** Shown are results during  
 647 blocking over Euro-Atlantic (left column), northern Russia (middle column) and North  
 648 Pacific (right column) for (a,b,c) BASE, (d,e,f) ozone difference between blocking and  
 649 non-blocking, (g,h,i) effect of BVOC emissions, (j,k,l) differences of effects of BVOC  
 650 emissions on ozone between blocking and non-blocking.

651



652

653 **Fig. 10 Probability distribution function of MDA8 ozone concentrations.** Shown  
 654 are results over North China (NC; left column) and central eastern China (CECN; right  
 655 column) during blocking events occurred at Euro-Atlantic sector (top), northern Russia  
 656 (middle) and North Pacific (bottom). The numbers on the top right of each panel  
 657 represent the MDA8 ozone enhancement between blocking and non-blocking (BASE  
 658 (BL-non\_BL)), effect of BVOC emissions during blocking (BL BVOC) and non-  
 659 blocking (non\_BL BVOC). The numbers on the bottom right of each panel show the

660 mean MDA8 ozone concentrations during blocking (in red) and non-blocking (in blue)  
661 for BASE and the case without BVOC emissions. Since ozone values in the non-  
662 blocking case is the same no matter where the blocking is, values for the non-blocking  
663 case are only listed on the top row. The solid and dashed blue lines are the same between  
664 middle, bottom rows and the top row.

665

**Conclusions**

**Discussion**

668 Through the combination of high-resolution Earth system models and observations,  
669 the effects of local meteorology and large-scale circulation on ozone concentrations are  
670 elucidated. Based on observations and focusing on eastern China, we identify that  
671 ozone pollution events are accompanied by anomalously high near-surface air  
672 temperature, increased downward surface solar radiation, reduced water vapor and  
673 decreased total cloud cover. We further find that blocking events over the Euro-Atlantic  
674 sector, northern Russia and the North Pacific behave differently in modulating ozone  
675 pollution in eastern China, controlled by the pathways of Rossby wave propagation.  
676 While blocking in all three regions plays the most significant role in central eastern  
677 China, blocking over northern Russia and the North Pacific may also impact the  
678 southern part of China. Over the North Pacific, the large high-pressure system seems to  
679 form a saddle-like structure, affecting widespread areas in southern China.

680 Moreover, blocking events could substantially trigger BVOC emission increases  
681 and aggravate ozone pollution. Numerical experiments reveal that under favorable  
682 meteorological conditions, such as heatwaves, BVOC emissions could play an even  
683 larger role in triggering ozone increases, particularly in areas with lower anthropogenic  
684 emissions. This highlights a potentially more critical role for BVOC emissions,  
685 especially when anthropogenic emissions are projected to decrease. This is the first  
686 attempt to link atmospheric blocking, BVOC emissions, and ozone pollution, which has  
687 important implications for future studies, particularly those associated with the  
688 mechanisms of how large-scale circulations affect ozone concentrations under a

689 warming climate.

690

691

692 Our findings are subject to some uncertainties and limitations. In this study, the  
693 contribution of BVOC to ozone is not necessarily limited to VOC-limited regions but  
694 rather results from a combination of various effects. In VOC-limited regions, the  
695 increase in BVOCs has a clear promoting effect on ozone formation. Even in NOx-  
696 limited regions or areas with low BVOC emissions, the positive role of BVOC in ozone  
697 formation can still be observed, with one of the key reasons being the influence of  
698 atmospheric transport. In one of our previous studies (Wang et al., 2022), taking  
699 Shandong Province as an example, we found that although BVOC emissions in  
700 Shandong were relatively low, the impact of BVOC on ozone levels in the province  
701 could exceed 10 ppbv. Sensitivity numerical experiments revealed that biogenic  
702 emissions from southern China led to an increase in ozone, which was subsequently  
703 transported northeastward, contributing to the elevated ozone concentrations in  
704 Shandong.

705 In addition to the traditional VOC-limited and NOx-limited regimes, the  
706 inhibition effect of aerosol uptake on ozone production is also an important influencing  
707 factor (Kanaya et al., 2009; Li et al., 2019). In urban areas with relatively sufficient  
708 NOx but insufficient VOCs, the reaction between VOCs and OH generally has a greater  
709 impact on ozone than the effect of aerosol uptake (Song et al., 2020; Tang et al.,  
710 2017). In regions with relatively insufficient NOx and heavy pollution, such as parts of  
711 eastern China, the aerosol uptake of HO<sub>2</sub> may also become the dominant mechanism  
712 driving changes in ozone concentration (Ivatt et al. (2022). With future reductions in  
713 air pollution, the aerosol HO<sub>2</sub> uptake effect may weaken, which could, in turn, promote  
714 an increase in ozone. The impact of BVOCs on ozone in this study can be interpreted  
715 as the impact of ozone precursors such as VOCs and NOx on ozone, as well as the effect  
716 of aerosol uptake. Future research could further explore isolating the impact of HO<sub>2</sub>  
717 aerosol uptake on ozone, which would help enhance the understanding of the

718 [mechanisms and sources of BVOC effects on ozone. Meanwhile, future ozone pollution](#)  
719 [management needs to consider both the emission of ozone precursors and the potential](#)  
720 [weakening effect of aerosol reductions.](#)

721 [Using high-resolution models can better distinguish the spatial heterogeneity of](#)  
722 [BVOC emissions, thereby facilitating the evaluation of their impact on atmospheric](#)  
723 [pollutants. The differences in BVOC emissions between the high-resolution and low-](#)  
724 [resolution models in this study arise from both resolution differences and](#)  
725 [meteorological variations. This study has not separated these factors, and further](#)  
726 [investigation is needed to understand the effects caused solely by changes in resolution.](#)

727 [Considering that halogens play an important role in affecting tropospheric ozone](#)  
728 [concentrations, we have conducted preliminary tests using Community Earth System](#)  
729 [Model \(CESM\) version 2.2, referencing relevant studies \(e.g., \(Badia et al., 2021; Li et](#)  
730 [al., 2022; Saiz-Lopez et al., 2023\)\). The atmospheric and land components are CAM6](#)  
731 [and CLM5, respectively. The ocean and sea ice data are prescribed from the Merged](#)  
732 [Hadley-NOAA/OI Sea Surface Temperature & Sea-Ice Concentration dataset \(Hurrell](#)  
733 [et al., 2008\). To improve the accuracy of meteorological simulations, we applied the](#)  
734 [nudging method. The reanalysis data used is the 6-hourly reanalysis dataset from the](#)  
735 [Modern-Era Retrospective Analysis for Research and Applications, Version 2](#)  
736 [\(MERRA-2\). The variables nudged include air temperature, eastward wind, and](#)  
737 [northward wind. We selected the period from January to December 2019 as the study](#)  
738 [period \(with a spin-up time of six months\). The model was configured with low-](#)  
739 [resolution \(~1°\) simulations. The emissions are based on the Community Emissions](#)  
740 [Data System \(CEDS\) emission dataset under the SSP370 scenario, and two sets of](#)  
741 [numerical simulations were conducted: one without complex halogen chemistry and](#)  
742 [the other with complex halogen chemistry included \(details on halogen reactions in](#)  
743 [Saiz-Lopez et al. \(2023\)\).](#)

744 [Fig S11 shows that compared to the case without halogen chemistry, the inclusion](#)  
745 [of halogen chemistry substantially reduces the simulated ozone concentrations for the](#)  
746 [U.S., Europe, and Eastern China. Relative to the observations, when examining this](#)

747 single year of simulation, the average bias is reduced from 10% (7%-13% for the three  
748 regions) to 3% (2%-6% for the three regions). Most of the improvement occurs in winter,  
749 spring, and fall, while changes during summer are relatively smaller.

750 However, note that this is only a one-year simulation, and more future work is  
751 needed to fully examine the effectiveness of halogen chemistry on ozone. For instance,  
752 useful tests include firstly the simulations of multi-year instead of only one-year.  
753 Secondly, it is useful to conduct high-resolution Earth system simulations (e.g., 25 km)  
754 to take advantage of finer resolution emissions and the spatial heterogeneities in  
755 emissions. Thirdly, this study primarily focuses on large regional scales; future  
756 evaluations can further assess simulations over smaller regions and specific ozone  
757 pollution episodes.

758 The above tests were conducted for Cl, Br, and I. In the future, individual halogens,  
759 such as iodine, could be tested separately. Iodine serves as an important ozone sink  
760 (Alicke et al., 1999; Pound et al., 2023; Saiz-Lopez et al., 2012; Sherwen et al., 2016).  
761 Based on Sherwen et al. (2016), the impact of iodine on ozone is primarily observed  
762 over tropical oceans, with relatively limited effects on near-surface ozone. More  
763 information can be investigated in future studies.

764  
765 **Data availability.** The CESM model output data are available from the iHESP data  
766 portal ([https://ihesp.github.io/archive/products/ihesp-products/data-](https://ihesp.github.io/archive/products/ihesp-products/data-release/DataRelease_Phase2.html)  
767 [release/DataRelease\\_Phase2.html](https://ihesp.github.io/archive/products/ihesp-products/data-release/DataRelease_Phase2.html)).

768 **Author contributions**

769 Y.G. conceived the project and designed the method, W.K. performed the analysis and  
770 drafted the manuscript, X.G., X.A. helped on the analysis, D.T, W.L., M.C., X.G., S.Z.,  
771 H.G., L.W. helped on the interpretation of the results. All authors contributed to the  
772 writing of the manuscript.

773

774 **Competing interests**

设置了格式: 字体: 非加粗

带格式的: 两端对齐, 缩进: 首行缩进: 2 字符, 定义网格后自动调整右缩进, 行距: 1.5 倍行距, 调整中文与西文文字的间距, 调整中文与数字的间距

775 The authors declare that they have no conflicts of interest.

776

777

## 778 Acknowledgements

779 This work was supported by the National Natural Science Foundation of China  
780 (42122039, 42375189), the Science and Technology Innovation Project of Laoshan  
781 Laboratory (LSKJ202300401, LSKJ202202201) and Hainan Provincial Joint Project of  
782 Sanya Yazhou Bay Science and Technology City (2021JJLH0050).

783

## 784 References

785 [Aliche, B., Hebestreit, K., Stutz, J., and Platt, U.: Iodine oxide in the marine boundary layer, \*Nature\*, 397, 572-573, 10.1038/17508, 1999.](#)

786 Amano, M., Tachibana, Y., and Ando, Y.: Consideration of whether a climatic regime shift has prevented  
787 the occurrence of a cold summer in northeast Eurasia since 2010, [Journal of Climate](#), 10.1175/jcli-d-23-0191.1, 2023.

788 [Badia, A., Iglesias-Suarez, F., Fernandez, R. P., Cuevas, C. A., Kinnison, D. E., Lamarque, J.-F., Griffiths, P. T., Tarasick, D. W., Liu, J., and Saiz-Lopez, A.: The Role of Natural Halogens in Global Tropospheric Ozone Chemistry and Budget Under Different 21st Century Climate Scenarios, \*Journal of Geophysical Research: Atmospheres\*, 126, e2021JD034859, 10.1029/2021JD034859, 2021.](#)

789 Barnes, E. A., and Fiore, A. M.: Surface ozone variability and the jet position: Implications for projecting  
790 future air quality, [Geophysical Research Letters, Geophys. Res. Lett.](#), 40, 2839-2844, 10.1002/grl.50411, 2013.

791 Barriopedro, D., García-Herrera, R., Lupo, A. R., and Hernández, E.: A Climatology of Northern  
792 Hemisphere Blocking, [Journal of Climate](#), 19, 1042-1063, 10.1175/JCLI3678.1, 2006.

793 Barriopedro, D., Fischer, E. M., Luterbacher, J., Trigo, R., and Garcia-Herrera, R.: The Hot Summer of  
794 2010: Redrawing the Temperature Record Map of Europe, *Science*, 332, 220-224,  
795 10.1126/science.1201224, 2011.

796 Brauer, M., Casadei, B., Harrington, R. A., Kovacs, R., Sliwa, K., and Grp, W. A. P. E.: Taking a stand  
797 against air pollution - the impact on cardiovascular disease, [European Eur. Heart Journal](#), 42, 1460-  
798 1463, 10.1093/eurheartj/ehaa1025, 2021.

800 Cattiaux, J., Vautard, R., Cassou, C., Yiou, P., Masson-Delmotte, V., and Codron, F.: Winter 2010 in  
801 Europe: A cold extreme in a warming climate, [Geophysical Research Letters, Geophys. Res. Lett.](#), 37,  
802 10.1029/2010gl044613, 2010.

803 Chang, P., Zhang, S., Danabasoglu, G., Yeager, S. G., Fu, H., Wang, H., Castruccio, F. S., Chen, Y.,  
804 Edwards, J., Fu, D., Jia, Y., Laurindo, L. C., Liu, X., Rosenbloom, N., Small, R. J., Xu, G., Zeng, Y.,

810 Zhang, Q., Bacmeister, J., Bailey, D. A., Duan, X., DuVivier, A. K., Li, D., Li, Y., Neale, R., Stössel, A.,  
811 Wang, L., Zhuang, Y., Baker, A., Bates, S., Dennis, J., Diao, X., Gan, B., Gopal, A., Jia, D., Jing, Z., Ma,  
812 X., Saravanan, R., Strand, W. G., Tao, J., Yang, H., Wang, X., Wei, Z., and Wu, L.: An Unprecedented  
813 Set of High-Resolution Earth System Simulations for Understanding Multiscale Interactions in Climate  
814 Variability and Change, *Journal of Advances in Modeling J. Adv. Model. Earth Systems*, 12,  
815 e2020MS002298, 10.1029/2020MS002298, 2020.

816 Christoudias, T., Pozzer, A., and Lelieveld, J.: Influence of the North Atlantic Oscillation on air pollution  
817 transport, *Atmos. Chem. Phys.*, 12, 869-877, 10.5194/acp-12-869-2012, 2012.

818 Churkina, G., Kuik, F., Bonn, B., Lauer, A., Grote, R., Tomiak, K., and Butler, T. M.: Effect of VOC  
819 Emissions from Vegetation on Air Quality in Berlin during a Heatwave, *Environmental Science &*  
820 *Technology Environ. Sci. Technol.*, 51, 6120-6130, 10.1021/acs.est.6b06514, 2017.

821 Clifton, O. E., Fiore, A. M., Massman, W. J., Baublitz, C. B., Coyle, M., Emberson, L., Fares, S., Farmer,  
822 D. K., Gentine, P., Gerosa, G., Guenther, A. B., Helmig, D., Lombardozzi, D. L., Munger, J. W., Patton,  
823 E. G., Pusede, S. E., Schwede, D. B., Silva, S. J., Sörgel, M., Steiner, A. L., and Tai, A. P. K.: Dry  
824 Deposition of Ozone Over Land: Processes, Measurement, and Modeling, *Reviews of Geophysics Rev*  
825 *Geophys.*, 58, e2019RG000670, 10.1029/2019RG000670, 2020.

826 Deitrick, R., and Goldblatt, C.: Effects of ozone levels on climate through Earth history, *Climate of*  
827 *theClim Past*, 19, 1201-1218, 10.5194/cp-19-1201-2023, 2023.

828 Dentener, F., Keating, T., and Akimoto, H.: Hemispheric transport of air pollution 2010, Part A - Ozone  
829 and Particulate Matter, *Air Pollution Studies No.17*. United Nations, New York and Geneva, 2010.

830 Ding, F., and Li, C.: Subtropical westerly jet waveguide and winter persistent heavy rainfall in south  
831 China, *Journal of Geophysical Research: Atmospheres*, 122, 7385-7400, 10.1002/2017JD026530, 2017.

832 Dunker, A. M., Koo, B., and Yarwood, G.: Contributions of foreign, domestic and natural emissions to  
833 US ozone estimated using the path-integral method in CAMx nested within GEOS-Chem, *Atmospheric*  
834 *Chemistry and Physics Atmos. Chem. Phys.*, 17, 12553-12571, 10.5194/acp-17-12553-2017, 2017.

835 Emberson, L. D., Pleijel, H., Ainsworth, E. A., van den Berg, M., Ren, W., Osborne, S., Mills, G., Pandey,  
836 D., Dentener, F., Büker, P., Ewert, F., Koeble, R., and Van Dingenen, R.: Ozone effects on crops and  
837 consideration in crop models, *European Journal of Agronomy Eur. J. Agron.*, 100, 19-34,  
838 10.1016/j.eja.2018.06.002, 2018.

839 Emmons, L. K., Schwantes, R. H., Orlando, J. J., Tyndall, G., Kinnison, D., Lamarque, J.-F., Marsh, D.,  
840 Mills, M. J., Tilmes, S., Bardeen, C., Buchholz, R. R., Conley, A., Gettelman, A., Garcia, R., Simpson,  
841 I., Blake, D. R., Meinardi, S., and Pétron, G.: The Chemistry Mechanism in the Community Earth System  
842 Model Version 2 (CESM2), *Journal of Advances in Modeling J. Adv. Model. Earth Systems*, 12,  
843 e2019MS001882, 10.1029/2019MS001882, 2020.

844 Fu, T.-M., and Tian, H.: Climate Change Penalty to Ozone Air Quality: Review of Current  
845 Understandings and Knowledge Gaps, *Current Pollution Reports*, 5, 159-171, 10.1007/s40726-019-  
846 00115-6, 2019.

847 Fuller, R., Landrigan, P. J., Balakrishnan, K., Bathan, G., Bose-O'Reilly, S., Brauer, M., Caravanos, J.,  
848 Chiles, T., Cohen, A., Corra, L., Cropper, M., Ferraro, G., Hanna, J., Hanrahan, D., Hu, H., Hunter, D.,  
849 Janata, G., Kupka, R., Lanphear, B., Lichtveld, M., Martin, K., Mustapha, A., Sanchez-Triana, E.,  
850 Sandilya, K., Schaeffli, L., Shaw, J., Seddon, J., Suk, W., Téllez-Rojo, M. M., and Yan, C. H.: Pollution  
851 and health: a progress update, *Lancet Planetary Health*, 6, E535-E547, 10.1016/S2542-  
852 5196(22)00090-0, 2022.

853 Gao, Y., Fu, J. S., Drake, J. B., Liu, Y., and Lamarque, J. F.: Projected changes of extreme weather events  
854 in the eastern United States based on a high resolution climate modeling system, *Environmental Research  
855 Letters*, 7, 044025, 10.1088/1748-9326/7/4/044025, 2012.

856 Gao, Y., Zhang, J.-X., Yan, F., Leung, L. R., Luo, K., Zhang, Y., and Bell, M. L.: Nonlinear effect of  
857 compound extreme weather events on ozone formation over the United States, *Weather and Climate  
858 Extremes*, 30, 100285, 10.1016/j.wace.2020.100285, 2020.

859 Gao, Y., Yan, F., Ma, M., Ding, A., Liao, H., Wang, S., Wang, X., Zhao, B., Cai, W., Su, H., Yao, X., and  
860 Gao, H.: Unveiling the dipole synergic effect of biogenic and anthropogenic emissions on ozone  
861 concentrations, *Science of The Total Environment*, 818, 151722,  
862 10.1016/j.scitotenv.2021.151722, 2022.

863 Gao, Y., Wu, Y., Guo, X., Kou, W., Zhang, S., Leung, L. R., Chen, X., Lu, J., Diffenbaugh, N. S., Horton,  
864 D. E., Yao, X., Gao, H., and Wu, L.: More Frequent and Persistent Heatwaves Due To Increased  
865 Temperature Skewness Projected by a High-Resolution Earth System Model, *Geophysical Research  
866 Letters, Geophys. Res. Lett.*, 50, e2023GL105840, 10.1029/2023GL105840, 2023.

867 Gao, Y., Guo, X., Lu, J., Woolings, T., Chen, D., Guo, X., Kou, W., Zhang, S., Leung, L. R., Schiemann,  
868 R., Turner, A., O'Reilly, C., Guo, C., Li, J., Gao, H., and Wu, L.: Enhanced Simulation of Atmospheric  
869 Blocking with High-Resolution Earth System Models: Implications for Future Climate Scenarios, in  
870 review-a.

871 Gao, Y., Kou, W., Cheng, W., Guo, X., Qu, B., Wu, Y., Zhang, S., Liao, H., Chen, D., Leung, L. R., Wild,  
872 O., Zhang, J., Lin, G., Su, H., Cheng, Y., Pöschl, U., Pozzer, A., Zhang, L., Lamarque, J.-F., Guenther, A.  
873 B., Brasseur, G., Liu, Z., Lu, H., Li, C., Zhao, B., Wang, S., Huang, X., Pan, J., Liu, G., Liu, X., Lin, H.,  
874 Zhao, Y., Zhao, C., Meng, J., Yao, X., Gao, H., and Wu, L.: Reducing long-standing surface ozone  
875 overestimation in Earth system modelling by high-resolution simulation and dry deposition improvement,  
876 in review-b.

877 Gong, C., and Liao, H.: A typical weather pattern for ozone pollution events in North China, *Atmos.  
878 Chem. Phys.*, 19, 13725-13740, 10.5194/acp-19-13725-2019, 2019.

879 Gong, C., Liao, H., Zhang, L., Yue, X., Dang, R., and Yang, Y.: Persistent ozone pollution episodes in  
880 North China exacerbated by regional transport, *Environmental Pollution*, 265, 115056,  
881 10.1016/j.envpol.2020.115056, 2020.

882 Granier, C., Darras, S., Gon, H. D. v. d., Doubalova, J., Elguindi, N., Galle, B., M. Gauss, M., and  
883 Guevara, J.-P. J., J. Kuenen, C. Liousse, B. Quack, D. Simpson, K. Sindelarova, : The Copernicus

884 Atmosphere Monitoring Service global and regional emissions (April 2019 version), Copernicus  
885 Atmosphere Monitoring Service (CAMS) report, 10.24380/d0bn-kx16, 2019.

886 Guenther, A. B., Jiang, X., Heald, C. L., Sakulyanontvittaya, T., Duhl, T., Emmons, L. K., and Wang, X.:  
887 The Model of Emissions of Gases and Aerosols from Nature version 2.1 (MEGAN2.1): an extended and  
888 updated framework for modeling biogenic emissions, *Geoscientific Model Development*, 5, 1471-1492,  
889 10.5194/gmd-5-1471-2012, 2012.

890 Guion, A., Turquety, S., Cholakian, A., Polcher, J., Ehret, A., and Lathiere, J.: Biogenic isoprene  
891 emissions, dry deposition velocity, and surface ozone concentration during summer droughts, heatwaves,  
892 and normal conditions in southwestern Europe, [Atmospheric Chemistry and Physics](#), [Atmos. Chem. Phys.](#),  
893 23, 1043-1071, 10.5194/acp-23-1043-2023, 2023.

894 Guo, X., Gao, Y., Zhang, S., Wu, L., Chang, P., Cai, W., Zscheischler, J., Leung, L. R., Small, J.,  
895 Danabasoglu, G., Thompson, L., and Gao, H.: Threat by marine heatwaves to adaptive large marine  
896 ecosystems in an eddy-resolving model, *Nature Climate Change*, 12, 179-186, 10.1038/s41558-021-  
897 01266-5, 2022.

898 [Hurrell, J. W., Hack, J. J., Shea, D., Caron, J. M., and Rosinski, J.: A New Sea Surface Temperature and](#)  
899 [Sea Ice Boundary Dataset for the Community Atmosphere Model](#), *J. Climate*, 21, 5145-5153,

900 [10.1175/2008JCLI2292.1, 2008.](#)

901 [Ivatt, P. D., Evans, M. J., and Lewis, A. C.: Suppression of surface ozone by an aerosol-inhibited](#)  
902 [photochemical ozone regime](#), *Nature Geoscience*, 15, 536-540, 10.1038/s41561-022-00972-9, 2022.

903 Kalnay, E., Kanamitsu, M., Kistler, R., Collins, W., Deaven, D., Gandin, L., Iredell, M., Saha, S., White,  
904 G., Woollen, J., Zhu, Y., Chelliah, M., Ebisuzaki, W., Higgins, W., Janowiak, J., Mo, K. C., Ropelewski,  
905 C., Wang, J., Leetmaa, A., Reynolds, R., Jenne, R., and Joseph, D.: The NCEP/NCAR 40-Year Reanalysis  
906 Project, [Bulletin of the American Meteorological Society](#), *B. Am. Meteorol. Soc.*, 77, 437-472,  
907 10.1175/1520-0477(1996)077<0437:TNYRP>2.0.CO;2, 1996.

908 [Kanaya, Y., Pochanart, P., Liu, Y., Li, J., Tanimoto, H., Kato, S., Suthawaree, J., Inomata, S., Taketani,](#)  
909 [F., Okuzawa, K., Kawamura, K., Akimoto, H., and Wang, Z. F.: Rates and regimes of photochemical](#)  
910 [ozone production over Central East China in June 2006: a box model analysis using comprehensive](#)  
911 [measurements of ozone precursors](#), *Atmos. Chem. Phys.*, 9, 7711-7723, 10.5194/acp-9-7711-2009, 2009.

912 Kang, D. W., Aneja, V. P., Mathur, R., and Ray, J. D.: Nonmethane hydrocarbons and ozone in three rural  
913 southeast United States national parks: A model sensitivity analysis and comparison to measurements,  
914 [Journal of Geophysical Research Atmospheres](#), *J. Geophys. Res.-Atmos.*, 108, 4604,  
915 10.1029/2002jd003054, 2003.

916 Lamarque, J. F., Emmons, L. K., Hess, P. G., Kinnison, D. E., Tilmes, S., Vitt, F., Heald, C. L., Holland,  
917 E. A., Lauritzen, P. H., Neu, J., Orlando, J. J., Rasch, P. J., and Tyndall, G. K.: CAM-chem: description  
918 and evaluation of interactive atmospheric chemistry in the Community Earth System Model, *Geosci.*  
919 *Model Dev.*, 5, 369-411, 10.5194/gmd-5-369-2012, 2012.

920 Li, [K., Jacob, D. J., Liao, H., Shen, L., Zhang, Q., and Bates, K. H.: Anthropogenic drivers of 2013-2017](#)

921 [trends in summer surface ozone in China, Proc. Natl. Acad. Sci. U. S. A., 116, 422-427, 10.1073/pnas.1812168116, 2019.](#)

922

923 [Li, M., Liu, H., Geng, G-N., Hong, C-P., Liu, F., Song, Y., Tong, D., Zheng, B., Cui, H-Y., Man, H-Y., Zhang, Q., and He, K-B.: Anthropogenic emission inventories in China: a review, National Science Review, 4, 834-866, 10.1093/nsr/nwx150, 2017.](#)

924

925

926 [Li, Q., Fernandez, R. P., Hossaini, R., Iglesias-Suarez, F., Cuevas, C. A., Apel, E. C., Kinnison, D. E., Lamarque, J.-F., and Saiz-Lopez, A.: Reactive halogens increase the global methane lifetime and radiative forcing in the 21st century, Nat. Commun., 13, 2768, 10.1038/s41467-022-30456-8, 2022.](#)

927

928

929 [Li, R.-X., and Sun, J.-Q.: Interdecadal variability of the large-scale extreme hot event frequency over the middle and lower reaches of the Yangtze River basin and its related atmospheric patterns, Atmospheric and Oceanic Science Letters, 11, 63-70, 10.1080/16742834.2017.1335580, 2018.](#)

930

931

932 [Liu, L., Wu, B., and Ding, S.: On the Association of the Summertime Shortwave Cloud Radiative Effect in Northern Russia With Atmospheric Circulation and Climate Over East Asia, Geophysical Research Letters, Geophys. Res. Lett., 49, e2021GL096606, 10.1029/2021GL096606, 2022.](#)

933

934

935 [Lupo, A. R.: Atmospheric blocking events: a review, Annals of the New York Academy of Sciences, Ann. N. Y. Acad. Sci., 1504, 5-24, 10.1111/nyas.14557, 2021.](#)

936

937 [Ma, M., Gao, Y., Wang, Y., Zhang, S., Leung, L. R., Liu, C., Wang, S., Zhao, B., Chang, X., Su, H., Zhang, T., Sheng, L., Yao, X., and Gao, H.: Substantial ozone enhancement over the North China Plain from increased biogenic emissions due to heat waves and land cover in summer 2017, Atmos. Chem. Phys., 19, 12195-12207, 10.5194/acp-19-12195-2019, 2019.](#)

938

939

940

941 [Ma, M., Gao, Y., Ding, A., Su, H., Liao, H., Wang, S., Wang, X., Zhao, B., Zhang, S., Fu, P., Guenther, A. B., Wang, M., Li, S., Chu, B., Yao, X., and Gao, H.: Development and Assessment of a High-Resolution Biogenic Emission Inventory from Urban Green Spaces in China, Environmental Science & Technology, 56, 175-184, 10.1021/acs.est.1c06170, 2022.](#)

942

943

944

945 [Ma, M. C., Gao, Y., Wang, Y. H., Zhang, S. Q., Leung, L. R., Liu, C., Wang, S. X., Zhao, B., Chang, X., Su, H., Zhang, T. Q., Sheng, L. F., Yao, X. H., and Gao, H. W.: Substantial ozone enhancement over the North China Plain from increased biogenic emissions due to heat waves and land cover in summer 2017, Atmospheric Chemistry and Physics, 19, 12195-12207, 10.5194/acp-19-12195-2019, 2019.](#)

946

947

948

949 [Masato, G., Hoskins, B. J., and Woollings, T.: Winter and Summer Northern Hemisphere Blocking in CMIP5 Models, Journal of Climate, 26, 7044-7059, 10.1175/JCLI-D-12-00466.1, 2013.](#)

950

951 [Meehl, G. A., Tebaldi, C., Tilmes, S., Lamarque, J. F., Bates, S., Pendergrass, A., and Lombardozzi, D.: Future heat waves and surface ozone, Environmental Research Letters, 13, 064004, 10.1088/1748-9326/aabdc, 2018.](#)

952

953

954 [Mochizuki, T., Ikeda, F., and Tani, A.: Effect of growth temperature on monoterpene emission rates of Acer palmatum, Science of the Sci. Total Environment, Environ., 745, 140886, 10.1016/j.scitotenv.2020.140886, 2020.](#)

955

956

957 Mousavinezhad, S., Choi, Y., Pouyaei, A., Ghahremanloo, M., and Nelson, D. L.: A comprehensive  
958 investigation of surface ozone pollution in China, 2015–2019: Separating the contributions from  
959 meteorology and precursor emissions, *Atmospheric ResearchAtmos. Res.*, 257, 105599,  
960 10.1016/j.atmosres.2021.105599, 2021.

961 Nakamura, H., Nakamura, M., and Anderson, J. L.: The Role of High- and Low-Frequency Dynamics in  
962 Blocking Formation, *Monthly Mon. Weather ReviewRev.*, 125, 2074-2093, 10.1175/1520-  
963 0493(1997)125<2074:TROHAL>2.0.CO;2, 1997.

964 Nuvolone, D., Petri, D., and Voller, F.: The effects of ozone on human health, *Environmental Science  
965 and Pollution ResearchEnviron. Sci. Pollut. R.*, 25, 8074-8088, 10.1007/s11356-017-9239-3, 2018.

966 Opacka, B., Müller, J. F., Stavrakou, T., Bauwens, M., Sindelarova, K., Markova, J., and Guenther, A.  
967 B.: Global and regional impacts of land cover changes on isoprene emissions derived from spaceborne  
968 data and the MEGAN model, *Atmospheric Chemistry and PhysicsAtmos. Chem. Phys.*, 21, 8413-8436,  
969 10.5194/acp-21-8413-2021, 2021.

970 Parrish, D. D., Law, K. S., Staehelin, J., Derwent, R., Cooper, O. R., Tanimoto, H., Volz-Thomas, A.,  
971 Gilge, S., Scheel, H. E., Steinbacher, M., and Chan, E.: Long-term changes in lower tropospheric baseline  
972 ozone concentrations at northern mid-latitudes, *Atmospheric Chemistry and PhysicsAtmos. Chem. Phys.*,  
973 12, 11485-11504, 10.5194/acp-12-11485-2012, 2012.

974 Parrish, D. D., Derwent, R. G., and Faloona, I. C.: Long-term baseline ozone changes in the Western US:  
975 A synthesis of analyses, *Journal of the J. Air & Waste Management AssociationManage. Assoc.*, 71,  
976 1397-1406, 10.1080/10962247.2021.1945706, 2021a.

977 Parrish, D. D., Derwent, R. G., and Staehelin, J.: Long-term changes in northern mid-latitude  
978 tropospheric ozone concentrations: Synthesis of two recent analyses, *Atmospheric EnvironmentAtmos.  
979 Environ.*, 248, 118227, 10.1016/j.atmosenv.2021.118227, 2021b.

980 Pelly, J. L., and Hoskins, B. J.: A new perspective on blocking, *Journal of the Atmospheric SciencesJ.  
981 Atmos. Sci.*, 60, 743-755, 10.1175/1520-0469(2003)060<0743:Anpob>2.0.Co;2, 2003.

982 Pound, R. J., Durcan, D. P., Evans, M. J., and Carpenter, L. J.: Comparing the Importance of Iodine and  
983 Isoprene on Tropospheric Photochemistry, Geophys. Res. Lett., 50, e2022GL100997,  
984 10.1029/2022GL100997, 2023.

985 Pugh, T. A. M., Ashworth, K., Wild, O., and Hewitt, C. N.: Effects of the spatial resolution of climate  
986 data on estimates of biogenic isoprene emissions, *Atmospheric EnvironmentAtmos. Environ.*, 70, 1-6,  
987 10.1016/j.atmosenv.2013.01.001, 2013.

988 Saiz-Lopez, A., Plane, J. M. C., Baker, A. R., Carpenter, L. J., von Glasow, R., Gómez Martín, J. C.,  
989 McFigans, G., and Saunders, R. W.: Atmospheric Chemistry of Iodine, Chem. Rev., 112, 1773-1804,  
990 10.1021/cr200029u, 2012.

991 Saiz-Lopez, A., Fernandez, R. P., Li, Q., Cuevas, C. A., Fu, X., Kinnison, D. E., Tilmes, S., Mahajan, A.  
992 S., Gómez Martín, J. C., Iglesias-Suarez, F., Hossaini, R., Plane, J. M. C., Myhre, G., and Lamarque, J.-

993 [E.: Natural short-lived halogens exert an indirect cooling effect on climate, Nature, 618, 967-973, 10.1038/s41586-023-06119-z, 2023.](#)

995 Schneidereit, A., Schubert, S., Vargin, P., Lunkeit, F., Zhu, X., Peters, D. H. W., and Fraedrich, K.: Large-  
996 Scale Flow and the Long-Lasting Blocking High over Russia: Summer 2010, [Monthly Mon Weather](#)  
997 [ReviewRev](#), 140, 2967-2981, 10.1175/MWR-D-11-00249.1, 2012.

998 Schwierz, C., Croci-Maspoli, M., and Davies, H. C.: Perspicacious indicators of atmospheric blocking,  
999 [Geophysical Research Letters, Geophys. Res. Lett.](#), 31, 10.1029/2003gl019341, 2004.

1000 [Sherwen, T., Schmidt, J. A., Evans, M. J., Carpenter, L. J., Großmann, K., Eastham, S. D., Jacob, D. J., Dix, B., Koenig, T. K., Sinreich, R., Ortega, I., Volkamer, R., Saiz-Lopez, A., Prados-Roman, C., Mahajan, A. S., and Ordóñez, C.: Global impacts of tropospheric halogens \(Cl, Br, I\) on oxidants and composition in GEOS-Chem, Atmos. Chem. Phys., 16, 12239-12271, 10.5194/acp-16-12239-2016, 2016.](#)

1004 Sillmann, J., Kharin, V. V., Zhang, X., Zwiers, F. W., and Branaugh, D.: Climate extremes indices in the  
1005 CMIP5 multimodel ensemble: Part 1. Model evaluation in the present climate, [Journal of Geophysical](#)  
1006 [Research: Atmospheres](#), 118, 1716-1733, 10.1002/jgrd.50203, 2013.

1007 [Song, H., Chen, X., Lu, K., Zou, Q., Tan, Z., Fuchs, H., Wiedensohler, A., Moon, D. R., Heard, D. E., Baeza-Romero, M. T., Zheng, M., Wahner, A., Kiendler-Scharr, A., and Zhang, Y.: Influence of aerosol copper on HO<sub>2</sub> uptake: a novel parameterized equation, Atmos. Chem. Phys., 20, 15835-15850, 10.5194/acp-20-15835-2020, 2020.](#)

1011 Sui, C., Karpechko, A. Y., Vihma, T., Yu, L., and Feng, L.: Influence of the Ural High on Air Temperatures  
1012 over Eastern Europe and Northern China during Extended Winter, [Journal of Climate](#), 35, 1309-1325,  
1013 10.1175/JCLI-D-21-0523.1, 2022.

1014 Sun, W. X., Hess, P., Chen, G., and Tilmes, S.: How waviness in the circulation changes surface ozone:  
1015 a viewpoint using local finite-amplitude wave activity, [Atmospheric Chemistry and Physics, Atmos.](#)  
1016 [Chem. Phys.](#), 19, 12917-12933, 10.5194/acp-19-12917-2019, 2019.

1017 Takaya, K., and Nakamura, H.: A Formulation of a Phase-Independent Wave-Activity Flux for Stationary  
1018 and Migratory Quasigeostrophic Eddies on a Zonally Varying Basic Flow, [Journal of the Atmospheric](#)  
1019 [Sciences, J. Atmos. Sci.](#), 58, 608-627, 10.1175/1520-0469(2001)058<0608:AFOAPI>2.0.CO;2, 2001.

1020 [Tang, M., Huang, X., Lu, K., Ge, M., Li, Y., Cheng, P., Zhu, T., Ding, A., Zhang, Y., Gligorovski, S., Song, W., Ding, X., Bi, X., and Wang, X.: Heterogeneous reactions of mineral dust aerosol: implications for tropospheric oxidation capacity, Atmos. Chem. Phys., 17, 11727-11777, 10.5194/acp-17-11727-2017, 2017.](#)

1024 Tarasick, D., Galbally, I. E., Cooper, O. R., Schultz, M. G., Ancellet, G., Leblanc, T., Wallington, T. J.,  
1025 Ziemke, J., Liu, X., Steinbacher, M., Staehelin, J., Vigouroux, C., Hannigan, J. W., García, O., Foret, G.,  
1026 Zanis, P., Weatherhead, E., Petropavlovskikh, I., Worden, H., Osman, M., Liu, J., Chang, K. L., Gaudel,  
1027 A., Lin, M. Y., Granados-Muñoz, M., Thompson, A. M., Oltmans, S. J., Cuesta, J., Dufour, G., Thouret,  
1028 V., Hassler, B., Trickl, T., and Neu, J. L.: Tropospheric Ozone Assessment Report: Tropospheric ozone  
1029 from 1877 to 2016, observed levels, trends and uncertainties, [Elementa-Science of the Anthropocene, Sci](#)

1030 [Anthrop](#), 7, 39, 10.1525/elementa.376, 2019.

1031 Tonnesen, S., and Jeffries, H. E.: Inhibition of odd oxygen production in the carbon bond four and generic  
1032 reaction set mechanisms, [Atmospheric Environment](#); [Atmos. Environ.](#), 28, 1339-1349, 10.1016/1352-  
1033 2310(94)90281-X, 1994.

1034 Unger, N.: On the role of plant volatiles in anthropogenic global climate change, [Geophysical Research](#)  
1035 [Letters](#); [Geophys. Res. Lett.](#), 41, 8563-8569, 10.1002/2014gl061616, 2014.

1036 [Wang, H., Gao, Y., Sheng, L., Wang, Y., Zeng, X., Kou, W., Ma, M., and Cheng, W.: The Impact of](#)  
1037 [Meteorology and Emissions on Surface Ozone in Shandong Province, China, during Summer 2014-2019,](#)  
1038 [Int. J. Environ. Res. Public. Health](#), 19(11), 6758, 10.3390/ijerph19116758, 2022.

1039 Wang, H. L., Wu, K., Liu, Y. M., Sheng, B. S., Lu, X., He, Y. P., Xie, J. L., Wang, H. C., and Fan, S. J.:  
1040 Role of Heat Wave-Induced Biogenic VOC Enhancements in Persistent Ozone Episodes Formation in  
1041 Pearl River Delta, [Journal of Geophysical Research Atmospheres](#); [J. Geophys. Res.-Atmos.](#), 126,  
1042 e2020JD034317, 10.1029/2020JD034317, 2021.

1043 Weng, H., Lin, J., Martin, R., Millet, D. B., Jaeglé, L., Ridley, D., Keller, C., Li, C., Du, M., and Meng,  
1044 J.: Global high-resolution emissions of soil NO<sub>x</sub>, sea salt aerosols, and biogenic volatile organic  
1045 compounds, [Scientific Data](#), 7, 148, 10.1038/s41597-020-0488-5, 2020.

1046 Wiedinmyer, C., Kimura, Y., McDonald-Buller, E. C., Emmons, L. K., Buchholz, R. R., Tang, W., Seto,  
1047 K., Joseph, M. B., Barsanti, K. C., Carlton, A. G., and Yokelson, R.: The Fire Inventory from NCAR  
1048 version 2.5: an updated global fire emissions model for climate and chemistry applications, [Geosci.](#)  
1049 [Model Dev.](#), 16, 3873-3891, 10.5194/gmd-16-3873-2023, 2023.

1050 Woollings, T., Barriopedro, D., Methven, J., Son, S.-W., Martius, O., Harvey, B., Sillmann, J., Lupo, A.  
1051 R., and Seneviratne, S.: Blocking and its Response to Climate Change, [Current Climate Change Reports](#),  
1052 4, 287-300, 10.1007/s40641-018-0108-z, 2018.

1053 Xu, P., Wang, L., and Chen, W.: The British–Baikal Corridor: A Teleconnection Pattern along the  
1054 Summertime Polar Front Jet over Eurasia, [Journal of Climate](#), 32, 877-896, 10.1175/JCLI-D-18-0343.1,  
1055 2019.

1056 Yang, X., Zeng, G., Iyakaremye, V., and Zhu, B.: Effects of different types of heat wave days on ozone  
1057 pollution over Beijing-Tianjin-Hebei and its future projection, [Science of The Sci.](#) [Total](#)  
1058 [Environment](#); [Environ.](#), 837, 155762, 10.1016/j.scitotenv.2022.155762, 2022.

1059 Yang, Y., Liao, H., and Li, J.: Impacts of the East Asian summer monsoon on interannual variations of  
1060 summertime surface-layer ozone concentrations over China, [Atmos. Chem. Phys.](#), 14, 6867–6879,  
1061 10.5194/acp-14-6867-2014, 2014.

1062 Yang, Y., Zhou, Y., Wang, H., Li, M., Li, H., Wang, P., Yue, X., Li, K., Zhu, J., and Liao, H.:  
1063 Meteorological characteristics of extreme ozone pollution events in China and their future predictions,  
1064 [Atmos. Chem. Phys.](#), 24, 1177-1191, 10.5194/acp-24-1177-2024, 2024.

1065 Yao, Y., Zhuo, W., Gong, Z., Luo, B., Luo, D., Zheng, F., Zhong, L., Huang, F., Ma, S., Zhu, C., and  
1066 Zhou, T.: Extreme Cold Events in North America and Eurasia in November-December 2022: A Potential  
1067 Vorticity Gradient Perspective, *Advances in Atmospheric Sciences*[\*Adv. Atmos. Sci.\*](#), 40, 953-962,  
1068 10.1007/s00376-023-2384-3, 2023.

1069 Yin, Z., Wang, H., Li, Y., Ma, X., and Zhang, X.: Links of climate variability in Arctic sea ice, Eurasian  
1070 teleconnection pattern and summer surface ozone pollution in North China, *Atmos. Chem. Phys.*, 19,  
1071 3857-3871, 10.5194/acp-19-3857-2019, 2019.

1072 Zeng, X. R., Gao, Y., Wang, Y. H., Ma, M. C., Zhang, J. X., and Sheng, L. F.: Characterizing the distinct  
1073 modulation of future emissions on summer ozone concentrations between urban and rural areas over  
1074 China, *Science of the Sci.* *Total Environment*[\*Environ.\*](#), 820, 153324, 10.1016/j.scitotenv.2022.153324,  
1075 2022.

1076 [Zhang, J., Gao, Y., Luo, K., Leung, L. R., Zhang, Y., Wang, K., and Fan, J.: Impacts of compound extreme](#)  
1077 [weather events on ozone in the present and future, \*Atmos. Chem. Phys.\*, 18, 9861-9877, 10.5194/acp-18-](#)  
1078 [9861-2018, 2018.](#)

1079 Zhang, J., Gao, Y., Leung, L. R., Luo, K., Wang, M., Zhang, Y., Bell, M. L., and Fan, J.: Isolating the  
1080 modulation of mean warming and higher-order temperature changes on ozone in a changing climate over  
1081 the contiguous United States, *Environmental Research Letters*, 17, 094005, 10.1088/1748-9326/ac8695,  
1082 2022.

1083 [Zhang, J. X., Gao, Y., Luo, K., Leung, L. R., Zhang, Y., Wang, K., and Fan, J. R.: Impacts of compound](#)  
1084 [extreme weather events on ozone in the present and future, \*Atmospheric Chemistry and Physics\*, 18,](#)  
1085 [9861-9877, 10.5194/acp-18-9861-2018, 2018.](#)

1086 [Zhang, R., Cohan, A., Bazar, A. P., and Cohan, D. S.: Source apportionment of biogenic contributions](#)  
1087 [to ozone formation over the United States, \*Atmospheric Environment\*\[\\*Atmos. Environ.\\*\]\(#\), 164, 8-19,](#)  
1088 [10.1016/j.atmosenv.2017.05.044, 2017.](#)

1089 Zohdirad, H., Jiang, J. H., Aksoyoglu, S., Namin, M. M., Ashrafi, K., and Prevot, A. S. H.: Investigating  
1090 sources of surface ozone in central Europe during the hot summer in 2018: High temperatures, but not  
1091 so high ozone, *Atmospheric Environment*[\*Atmos. Environ.\*](#), 279, 119099,  
1092 10.1016/j.atmosenv.2022.119099, 2022.

1093